

UC San Diego

UC San Diego Previously Published Works

Title

The SMC-family Wadjet complex protects bacteria from plasmid transformation by recognition and cleavage of closed-circular DNA.

Permalink

<https://escholarship.org/uc/item/0vz1j73k>

Journal

Molecular Cell, 82(21)

Authors

Gu, Yajie
Gao, Yong-Qi
Ego, Kaori
et al.

Publication Date

2022-11-03

DOI

10.1016/j.molcel.2022.09.008

Peer reviewed



Published in final edited form as:

Mol Cell. 2022 November 03; 82(21): 4145–4159.e7. doi:10.1016/j.molcel.2022.09.008.

The SMC-family Wadjet complex protects bacteria from plasmid transformation by recognition and cleavage of closed-circular DNA

Amar Deep^{1,†}, Yajie Gu^{1,†}, Yong-Qi Gao¹, Kaori M. Ego^{1,‡}, Mark A. Herzik Jr.², Huilin Zhou¹, Kevin D. Corbett^{1,3,*}

¹Department of Cellular and Molecular Medicine, University of California, San Diego, La Jolla, California, 92093, USA.

²Department of Chemistry and Biochemistry, University of California, San Diego, La Jolla, California, 92093, USA.

³Lead Contact

SUMMARY

Self versus non-self discrimination is a key element of innate and adaptive immunity across life. In bacteria, CRISPR-Cas and restriction-modification systems recognize non-self nucleic acids through their sequence and their methylation state, respectively. Here we show that the Wadjet defense system recognizes DNA topology to protect its host against plasmid transformation. Combining cryoelectron microscopy with crosslinking mass spectrometry, we show that Wadjet forms a complex similar to the bacterial condensin complex MukBEF, with a novel nuclease subunit similar to a type II DNA topoisomerase. Wadjet specifically cleaves closed-circular DNA in a reaction requiring ATP hydrolysis by the SMC ATPase subunit JetC, suggesting that the complex could use DNA loop extrusion to sense its substrate's topology, then specifically activate the nuclease subunit JetD to cleave plasmid DNA. Overall, our data reveal how bacteria have co-opted a DNA maintenance machine to specifically recognize and destroy foreign DNAs through topology sensing.

Graphical Abstract

*Correspondence: kcorbett@ucsd.edu.

‡Current address: ChenMed, Plantation, Florida, 33317, USA

†These authors contributed equally

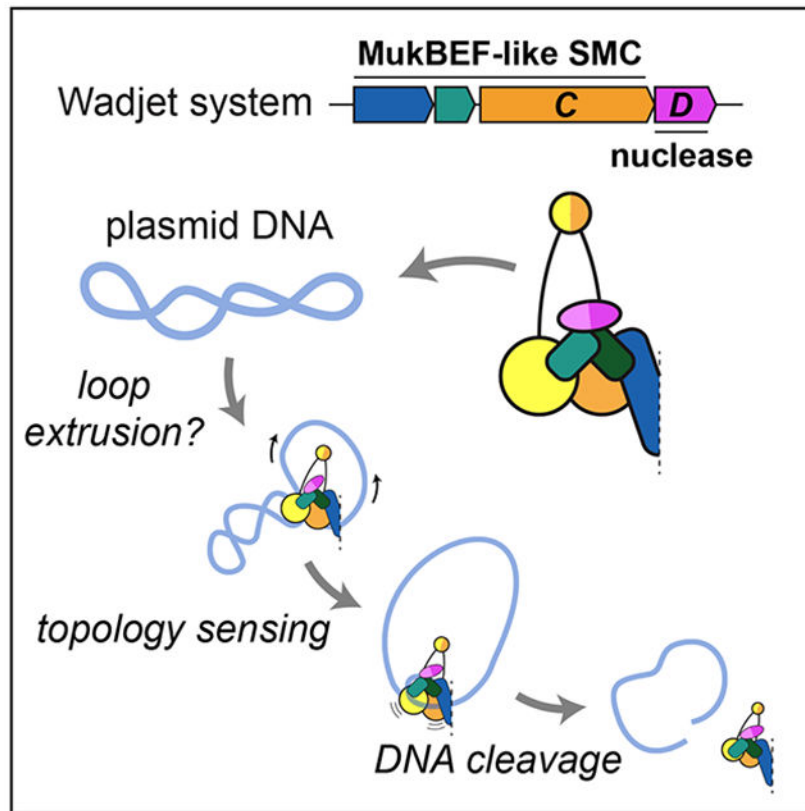
AUTHOR CONTRIBUTIONS

Conceptualization, A.D., and K.D.C.; Methodology, A.D., Y.G., and K.D.C.; Experimental Investigation, A.D., Y.G., Y-Q.G., K.M.E., and K.D.C.; Writing–Original Draft, A.D., and K.D.C.; Writing–Review & Editing, A.D., Y.G., M.A.H.J., H.Z., and K.D.C.; Visualization, A.D., and K.D.C.; Supervision, M.A.H.J., H.Z., and K.D.C.; Project Administration, K.D.C.; Funding Acquisition, M.A.H.J., H.Z., and K.D.C.

DECLARATION OF INTEREST

The authors declare no competing interests.

Publisher's Disclaimer: This is a PDF file of an unedited manuscript that has been accepted for publication. As a service to our customers we are providing this early version of the manuscript. The manuscript will undergo copyediting, typesetting, and review of the resulting proof before it is published in its final form. Please note that during the production process errors may be discovered which could affect the content, and all legal disclaimers that apply to the journal pertain.



eTOC BLURB

The bacterial Wadjet defense system protects its host cell from transformation by plasmids. Combining biochemical analysis and structure determination by cryo-EM, Deep et al. show that Wadjet recognizes and cleaves closed-circular DNA by coupling an SMC-family DNA motor activity to the specific activation of a homodimeric endonuclease.

Keywords

Wadjet defense system; Structural Maintenance of Chromosomes (SMC) complexes; bacterial defense systems; anti-plasmid defense system; EptABCD; MksBEFG; MukBEF; toprim domain; DNA topology; DNA loop extrusion

INTRODUCTION

Bacteria exist in a constant evolutionary arms race with other bacteria, bacteriophages, and parasitic DNA elements like plasmids (Granato et al., 2019; Stern and Sorek, 2011). To defend themselves against these threats, bacteria have evolved a variety of pathways that can neutralize foreign nucleic acids or trigger cell death in order to limit the spread of infection (Arber and Linn, 1969; Fineran et al., 2009; Lau et al., 2020; Millman et al., 2020). The availability of tens of thousands of bacterial genomes has enabled the recent computational identification of myriad putative defense systems (Doron et al., 2018; Gao et al., 2020; Millman et al., 2022). While the molecular mechanisms of several anti-phage

defense systems have recently been outlined, mechanistic understanding of anti-plasmid defense systems, including the widespread Wadjet system (named after an ancient Egyptian protector deity) and two recently discovered systems in *Vibrio cholerae*, DdmABC and DdmDE, has lagged behind (Doron et al., 2018; Gao et al., 2020; Jaskólska et al., 2022).

The four-gene Wadjet system (*jetABCD*) is present in ~6% of sequenced bacterial genomes, and strongly suppresses plasmid-mediated transformation of its host (Doron et al., 2018). Wadjet is equivalent to the previously-identified efficient plasmid transformation (*eptABCD*) system in *Mycobacterium smegmatis*, mutations in which result in a $>10^5$ -fold increase in plasmid transformation efficiency in this bacterium (Panas et al., 2014; Snapper et al., 1990). The Wadjet and ept systems are also equivalent to sporadically-distributed MukBEF-like SMC *mksBEFG* operons (Petrushenko et al., 2011), which have been implicated in plasmid maintenance and copy number control rather than anti-plasmid defense (Böhm et al., 2020).

The Wadjet proteins JetA, JetB, and JetC show sequence similarity to subunits of the bacterial condensin complex MukBEF, a member of the Structural Maintenance of Chromosomes (SMC) complex superfamily (Figure 1A) (Doron et al., 2018). SMC complexes are ubiquitous in prokaryotes and eukaryotes, and play key roles in genome organization, transcriptional control, and chromosome segregation (Davidson and Peters, 2021; Mäkelä and Sherratt, 2020a; Yatskevich et al., 2019). A general model for SMC complex function is that they bind DNA and processively extrude a DNA loop, thereby compacting and organizing chromosomes (Goloborodko et al., 2016). ATP-powered DNA loop extrusion has been directly demonstrated for the eukaryotic cohesin, condensin, and Smc5/6 complexes, lending support to this general model (Davidson and Peters, 2021; Davidson et al., 2019; Ganji et al., 2018; Kim et al., 2019; Pradhan et al., 2022). In γ -proteobacteria including *Escherichia coli*, MukBEF serves to condense and organize the genome, and to aid the individualization and segregation of replicated chromosomes (Danilova et al., 2007; Lioy et al., 2018; Niki et al., 1991). While DNA loop extrusion has not been directly demonstrated for MukBEF, the complex promotes long-range cis contacts within the bacterial chromosome (Lioy et al., 2018) and simulations show that processive bidirectional loop extrusion best explains its diverse roles in chromosome organization and segregation (Mäkelä and Sherratt, 2020b).

In MukBEF, a homodimer of the SMC ATPase subunit MukB forms the core DNA-binding motor of the complex. The MukB dimer assembles with two regulatory subunits, the kleisin-family protein MukF, and a homodimer of the KITE (kleisin interacting tandem winged-helix elements of SMC complexes) protein MukE (Badrinarayanan et al., 2012; Woo et al., 2009). MukE and MukF bind the MukB dimer asymmetrically, with MukF's central α -helical domain binding the "neck" region of one MukB protomer (denoted ν (nu)-MukB) and its C-terminal winged helix domain (C-WHD) binding the "cap" region of the second MukB protomer (denoted κ (kappa)-MukB). Finally, MukF homodimerization mediates the formation of a "MukBEF dimer" and the resulting MukF₂E₄B₄ complex is the functional form of MukBEF (Badrinarayanan et al., 2012; Rajasekar et al., 2019). Wadjet systems are predicted to encode three subunits analogous to MukB, MukE, and MukF, with an SMC ATPase subunit (JetC), a kleisin (JetA), and a KITE family protein (JetB; Figure 1A).

The fourth Wadjet subunit (JetD) shows distant homology to toprim (topoisomerase-primase) domain-containing nucleases, including the DNA-cleaving A subunit of archaeal topoisomerase VI (top6A) (Figure 1A). Toprim domains coordinate one or two Mg^{2+} ions and can support either DNA cleavage (in DNA topoisomerases and OLD-family nucleases) or nucleic acid synthesis (in bacterial DnaG-family primases) (Aravind et al., 1998). Mutation of one predicted Mg^{2+} -coordinating residue in the JetD toprim domain eliminates the system's ability to suppress plasmid transformation of a bacterial host, supporting a key role for this subunit in Wadjet function (Doron et al., 2018). While top6A possesses an N-terminal domain with the protein's active-site tyrosine residue (Aravind et al., 1998), JetD possesses an uncharacterized N-terminal domain of the DUF3322 family (Doron et al., 2018).

The pairing of an SMC-like complex with a putative DNA endonuclease subunit in Wadjet suggests that this system may recognize and eliminate plasmid DNA through a combination of DNA loop extrusion and DNA cleavage activities. Here, we reconstitute a functional Wadjet (JetABCD) complex *in vitro* and demonstrate that it specifically recognizes and cleaves closed-circular plasmid DNA, while showing no activity on equivalently-sized linear DNA. Both ATP hydrolysis by the SMC ATPase subunit JetC, and the catalytic site of the toprim-family nuclease subunit JetD, are essential for plasmid DNA cleavage *in vitro*. In cells, disruption of either JetC ATPase activity or the JetD catalytic site strongly suppresses Wadjet's anti-plasmid transformation activity. Together, these results suggest that Wadjet can specifically detect closed-circular DNA, potentially through a processive DNA loop extrusion mechanism, and couple this detection to activation of the JetD nuclease. Using cryoelectron microscopy (cryoEM) and cross-linking mass spectrometry, we constructed an overall model for the intact JetABCD complex that reveals how ATP-dependent dynamics of JetABC and its interaction with DNA could regulate the conformation and nuclease activity of JetD.

RESULTS

Wadjet specifically cleaves closed-circular DNA

To understand the biological role and molecular mechanism of Wadjet, we first established a plasmid transformation efficiency assay by chromosomally integrating an intact Wadjet system from *Bacillus cereus* strain Q1 into *Bacillus subtilis* (Figure 1A-B). As previously reported (Doron et al., 2018), Wadjet efficiently protects *B. subtilis* cells from transformation by an episomal plasmid, and this protection requires the ATPase activity of JetC (*jetC-EQ*: E1025Q Walker B motif mutation) and the presence of the putative nuclease subunit, JetD (Figure 1B).

We next sought to reconstitute the complex using recombinantly expressed proteins. After testing Wadjet systems from several bacteria, we succeeded in reconstituting the full JetABCD (MksBEFG) complex from a *Pseudomonas aeruginosa* strain, PA14 (Figure 1C, S1A, C). In addition to the canonical bacterial condensin SMC-ScpAB (Badrinarayanan et al., 2015), *P. aeruginosa* PA14 harbors a three-gene *mksBEF* operon (lacking the putative nuclease gene of full *mksBEFG* operons) identical to one that has been previously implicated in chromosomal DNA organization in a different *P. aeruginosa*

strain (Petrushenko et al., 2011), and the uncharacterized *mksBEFG/jetABCD* operon under study here. We first expressed and purified the putative SMC ATPase subunit JetC from this operon, which forms a stable homodimer on its own (Figure 1C, S1A, C). In keeping with their similarity to kleisin and KITE proteins, respectively, we could also purify a complex of JetA and JetB with 2:4 subunit stoichiometry (Figure 1C, S1A, C). This stoichiometry suggests that like their homologs MukF and MukE, JetA forms a kleisin homodimer and that each JetA subunit binds a homodimer of the KITE subunit JetB (Bürmann et al., 2021; Rajasekar et al., 2019; Woo et al., 2009). We mixed separately-purified JetC and JetAB to determine the stoichiometry of the overall JetABC complex. When we mixed the proteins in a 2 JetA:4 JetB:2 JetC ratio, we observed formation of a species consistent with a “monomeric” JetA₂B₄C₂ complex, plus excess JetA₂B₄ (Figure S1A, C). When we mixed the subunits in a 2 JetA:4 JetB:4 JetC ratio, we observed formation of a single species consistent with a “dimeric” JetA₂B₄C₄ complex (Figure S1A, C). Thus, like MukBEF, JetABC forms a dimer with two SMC subunit dimers. Finally, we purified JetD and found that it forms a homodimer (Figure 1C, S1A) and weakly binds the JetABC complex (Figure 1C). We found that reconstituted JetABC and JetABCD complexes show similar rates of ATP hydrolysis (~1-1.25 ATP min⁻¹), while isolated JetC shows very little activity (Figure S1D). Addition of supercoiled plasmid DNA to either JetABC or JetABCD did not significantly stimulate ATP hydrolysis (Figure S1D)

Based on the requirement for both JetC ATP hydrolysis and the presence of JetD for anti-plasmid transformation activity in cells, we hypothesized that Wadjet may recognize plasmid DNA through DNA binding and loop extrusion, and couple this recognition to DNA cleavage by JetD. To test this model, we incubated JetABCD with purified plasmid DNA, and found that the complex efficiently converts supercoiled plasmid DNA to a linear form (Figure 1D, lanes 5-7). Neither JetABC nor JetD alone is sufficient for DNA cleavage (Figure 1D, lanes 1-4). In addition, removal of ATP from the reaction buffer or disruption of JetC ATPase activity through an E1022Q Walker B motif mutation (equivalent to *B. cereus* Q1 JetC E1025Q) eliminates plasmid cleavage (Figure 1D, lanes 8-9). We next tested JetABCD activity on plasmid DNA that was pre-relaxed by incubation with topoisomerase I or with the nicking enzyme Nt.BsmAI, and found that JetABCD-mediated cleavage was unaffected (Figure 1D, lanes 12-15). Finally, we incubated JetABCD with NdeI-linearized plasmid DNA and observed no further DNA cleavage, even after extended incubation (Figure 1D, lanes 10-11). These results demonstrate that JetABCD senses the topology of DNA and specifically cleaves closed-circular DNA, regardless of supercoiling state, to generate a linear form.

To further probe the mechanism of Wadjet, we tested cleavage of two different-sized plasmids: a ~1 kb pUC-based plasmid and an ~8 kb pET-based plasmid (see **Methods**). Like the ~3 kb pUC18 plasmid tested above, we observed conversion of both plasmids to a linear form (Figure S2A-B). In time-course experiments, we observed that Wadjet cleaves both plasmids with similar kinetics, around 0.01 cleavage events per complex per minute (Figure S2C). The equivalent cleavage rates on different-size plasmids suggest that if Wadjet performs DNA loop extrusion as part of its recognition mechanism, then this activity is rapid compared to DNA cleavage. Indeed, eukaryotic SMC complexes extrude DNA loops at rates

of 0.5-2 kb/s (Davidson et al., 2019; Ganji et al., 2018), much faster than the rate we observe for Wadjet's plasmid cleavage activity. Finally, to address whether Wadjet shows sequence specificity for cleavage, we mapped cleavage sites on the ~1 kb plasmid by cloning the linear product of Wadjet cleavage into a second plasmid, followed by sequencing. These data show that Wadjet cleavage is essentially random, though we do observe a slight preference for the AT-rich origin of replication (Figure S2D-E).

JetABC adopts a MukBEF-like SMC architecture

To better understand the mechanistic basis for Wadjet function, we reconstituted and determined cryoelectron microscopy (cryoEM) structures of two *P. aeruginosa* PA14 JetABC subcomplexes. First, we generated a truncated JetC head-only construct (JetC^{head}) comprising residues 1-284 and 781-1101 joined by a short glycine-serine linker, and also containing the E1022Q Walker B motif mutation. This construct retains the ATPase head of JetC but lacks the bulk of the protein's coiled-coil and hinge domains (Figure 2A), and by SEC-MALS we find that JetC^{head} is primarily monomeric in solution (Figure S1B). We reconstituted a complex of full-length JetA, full-length JetB, and JetC^{head} and found by SEC-MALS that it adopts an overall stoichiometry of 2 JetA:4 JetB:2 JetC^{head} (Figure S1B). We determined a 2.95 Å resolution cryoEM structure of this complex, enabling us to confidently build models of all three subunits (Figure S3, Table 1).

At the core of the JetA-JetB-JetC^{head} structure is a dimer of the kleisin subunit JetA, which adopts an overall fold similar to MukF with an N-terminal winged-helix domain (WHD) followed by an α -helical dimerization domain. While the overall structure of the JetA dimer is similar to the MukF dimer, the JetA α -helical domain incorporates an additional α -helix compared to MukF, that we term the "crossover helix". The crossover helices mediate a domain swap between the two JetA protomers, such that while the overall dimer structure of JetA is similar to that of MukF, the position of each subunit's N-terminal WHD and α -helical domains are swapped (Figure S3H, J). The interleaved structure of the JetA dimer caused by the crossover helices dramatically increases the dimerization surface area of JetA (4,870 Å² per protomer) compared to MukF (3,700 Å² per protomer; calculated from PDB ID 1T98 (Fennell-Fezzie et al., 2005)).

Following the JetA α -helical domain is a short α -helix (residues 320-340) and an unstructured region (residues 341-375) that together bind and thread through a dimer of the KITE subunit JetB. The overall structure of JetB and its interaction with JetA is very similar to that of MukE, and the overall positioning of the JetB dimer with respect to JetA is also similar to the MukF-MukE complex (Figure S3I, K). We were unable to resolve the predicted C-terminal WHD of JetA in this structure.

Finally, the JetA-JetB-JetC^{head} structure reveals two copies of the JetC^{head} construct, one bound to either side of the JetA dimer (Figure S3F-G, S4A). Despite having added the non-hydrolyzable ATP analog ATP- γ -S during sample preparation, we observe no evidence for JetC head dimerization in this complex, suggesting that JetC requires its coiled-coil and hinge domains to form a stable dimer. The overall structure of the JetC ATPase head is similar to that of MukB, and more closely matches the conformation of MukB in its non-nucleotide bound (Apo) monomer state, rather than its ATP-bound dimer state (Figure

S4B-E). Thus, the JetA-JetB-JetC^{head} structure may represent the architecture of JetABC in its Apo state, prior to DNA or nucleotide binding (see below).

Next, we reconstituted a complex of *P. aeruginosa* PA14 JetA, JetB, and full-length JetC (E1022Q Walker B motif mutant) with a 65-bp double-stranded DNA. To isolate a nucleotide-bound state, we pre-incubated the complex with the non-hydrolyzable ATP analog ATP- γ -S. We collected a large cryoEM dataset from this sample (Figure S5, Table 1), from which we determined the structure of the intact JetABC complex missing only the JetC distal coiled-coil and hinge domains, and short disordered regions of JetA and JetB (Figure 2). By performing focused refinement on distinct regions of the complex, we resolved the dimerized JetC heads bound to the JetA C-terminal WHD (C-WHD) and DNA to a resolution of 3.3 Å (Figure 2E; density for bound ATP- γ -S in Figure 2F), the full JetC dimer to a resolution of 3.8 Å (Figure S5G), and a JetA₂B₄C₂ complex to a resolution of 4.1 Å (Figure 2B-C). Unlike a recent cryoEM analysis of bacterial MukBEF (Bürmann et al., 2021), we were unable to resolve the structure of a full JetABC dimer with 2 JetA:4 JetB:4 JetC stoichiometry, though our dataset did show strong evidence of these particles (see below). We built a near-complete molecular model of the JetA₂B₄C₂ complex (88%, 75%, and 65% of JetA, JetB, and JetC residues, respectively) by combining our high-resolution structures of JetA, JetB, and the JetC head with an AlphaFold2 (Jumper et al., 2021; Mirdita et al., 2022) model of the proximal coiled-coil region, which we further refined using ISOLDE molecular dynamics-based refinement (Croll, 2018) into a focused-refinement map of the coiled-coil regions (Figure 2D). This map also revealed weak density for the JetC distal coiled-coils, showing that the coiled-coils are bent ~90° between the proximal and distal regions (Figure 2D). Due to the apparent flexibility at the JetC coiled-coil elbow, we were unable to model the distal coiled-coil and hinge domains.

The overall structure of JetABC strongly resembles that of the related MukBEF complex, with some notable differences. As in MukBEF, the kleisin subunit JetA binds asymmetrically to the JetC dimer, with its central α -helical domain binding the neck region of the ν -JetC protomer and its C-WHD domain binding the cap region of the κ -JetC protomer (Figure 2B). We observe DNA bound asymmetrically to the top of the JetC head dimer in a near-identical manner as that previously observed for a DNA-bound complex of MukBEF (Bürmann et al., 2021). Whereas the DNA-bound structure of MukBEF showed a “clamped” conformation with the MukE dimer and the kleisin MukF wrapping over the bound DNA to tightly clamp it against MukB, our structure shows a distinct “unclamped” conformation with JetA and JetB rotated ~90° downward away from the JetC-bound DNA (Figure 2B, S6). In this conformation, JetB does not contact DNA, and the sole interactions between the JetAB subcomplex and the DNA-bound JetC are the small interface between JetA and the neck region of ν -JetC, and the interaction between JetA’s C-WHD and κ -JetC (Figure 2B).

Our structure of JetABC shows a single JetC dimer bound to a JetA₂B₄ complex. Our biochemical data, however, suggests that each JetA₂B₄ complex binds two JetC dimers to produce a JetA₂B₄C₄ complex similar to the previously observed MukBEF dimer (Figure S1A) (Bürmann et al., 2021). Supporting the formation of JetABC dimers, we identified a small set of particles in our cryoEM data that show a dimeric complex in an unclamped state

(Figure 2H, S7). In this state, the two JetC dimers are both in the unclamped conformation and are positioned roughly next to one another, oriented $\sim 45^\circ$ apart and facing opposite directions (Figure 2H, S7). Our inability to determine the JetABC dimer structure to high resolution is likely a combined result of flexibility in the unclamped conformation and likely instability of the larger dimeric complex during cryoEM sample preparation.

Structure of the Wadjet nuclease subunit JetD

Our biochemical data suggest that Wadjet functions by coupling ATP-powered DNA translocation or loop extrusion in JetABC to activation of latent nuclease activity in JetD. JetD is annotated as containing two domains of unknown function, a completely uncharacterized N-terminal DUF3322 domain (sometimes annotated as DUF3323) and a C-terminal DUF2220 domain (sometimes annotated as DUF2399) with distant homology to the “toprim” domain found in DNA topoisomerases, primases, and OLD family nucleases (Figure 1A) (Doron et al., 2018). To better understand the architecture of JetD and its possible nuclease activity, we determined a ~ 3.7 Å-resolution structure of the *P. aeruginosa* PA14 JetD homodimer by cryoEM (Figure 3A-C, S8, Table 1). In the structure, JetD forms a homodimer with the N-terminal DUF3322 domains extending upward from the dimerized C-terminal domains (Figure 3B-C). As predicted by its sequence, the JetD C-terminal domain displays close structural homology to known toprim domains, including that of archaeal topoisomerase VI-A (Figure 3E) (top6A; Ca r.m.s.d. 4.0 Å) (Corbett et al., 2007; Graille et al., 2008; Nichols et al., 1999) and OLD-family nucleases (Figure S8L) (Schiltz et al., 2019). Like top6A, dimerization of the JetD toprim domain results in a cup-shaped symmetric homodimer with a central cleft that likely binds DNA (Figure 3C). Comparison of the JetD and top6A toprim domains reveals a conserved putative active site comprising a cluster of three acidic residues (E248, D291, and D293) that together likely coordinate a Mg^{2+} ion (Figure 3E). While top6A possesses a conserved tyrosine residue on its N-terminal 5Y-CAP domain that attacks the DNA backbone to mediate reversible DNA cleavage (Bergerat et al., 1997; Keeney et al., 1997; Nichols et al., 1999), JetD instead possesses a highly-conserved glutamate residue (E365) near the C-terminus of the toprim domain that may serve as a general acid to polarize a water molecule for nucleophilic attack on the DNA backbone (Figure 3E). All four of these acidic residues are absolutely conserved in JetD proteins. A fifth acidic residue, E363, is also highly conserved in JetD and may also play a role in catalysis. The architecture of the putative JetD active site suggests that the protein binds DNA similarly to top6A, but in contrast to the reversible DNA cleavage mechanism of top6A, JetD would instead irreversibly cleave the two DNA strands.

The N-terminal DUF3322 domains of JetD form extended arms that reach upward and cross above the putative DNA-binding cleft created by the toprim domain dimer (Figure 3C). Despite sharing no detectable sequence homology with top6A, we find that the C-terminal subdomain of this region shows structural homology to the N-terminal 5Y-CAP domain of top6A (Figure 3D). The top6A 5Y-CAP domain is named because of its homology to CAP (catabolite activator protein), and the fact that it contains the catalytic tyrosine residue that becomes covalently linked to the 5' end of DNA during catalysis (Nichols et al., 1999). The equivalent domain of JetD, which we term CAP, instead contains a pair of highly-conserved basic amino acids – R162 and K172 in *P. aeruginosa* PA14 JetD – that may be involved

in DNA binding (Figure 3D). The CAP domains are rigidly folded against the N-terminal subdomain of the JetD DUF3322 domain, which we term the “Arm” domain, and flexibly linked to the C-terminal toprim domain (Figure 3D).

As noted above, our structure shows the JetD N-terminal domains crossed above the cleft defined by the toprim domain dimer, likely preventing DNA binding (Figure 3C). Indeed, we tested for DNA binding by purified JetD using multiple methods, and could not detect an association (not shown). We modeled a putative active state of JetD by overlaying the JetD CAP domains on the 5Y-CAP domains of the top6A dimer, resulting in a dramatically more open conformation of the JetD dimer than we imaged by cryoEM (Figure 4A-B). We could model a DNA double helix binding across the toprim domain dimer, resulting in juxtaposed active sites positioned to cleave the complementary DNA strands as in top6A (Figure 4B). This model also positions the JetD CAP domains such that R162 and K172 are oriented toward the bound DNA (Figure 4C). To test this model and determine the role of the putative JetD active site in catalysis, we first reconstituted *P. aeruginosa* PA14 JetABCD complexes with alanine substitutions in residues E248, D291, and E365. The E248A and D291A mutations strongly suppressed plasmid cleavage, consistent with their putative role in Mg²⁺ binding (Figure 4D-E). Mutation of E365 to alanine completely eliminated DNA cleavage, consistent with an essential role for this residue in catalysis (Figure 4E). Finally, mutation of K172 also strongly suppressed plasmid cleavage, supporting a model in which the JetD CAP domain participates directly in either DNA binding or catalysis (Figure 4E). We were unable to test the role of R162 in catalysis due to insolubility of the JetD R162A mutant protein (not shown). Finally, we found that mutation of the equivalent active site residues in *Bacillus cereus* Q1 JetD effectively eliminates the system’s ability to protect *B. subtilis* cells from plasmid transformation (Figure 4F). Thus, the JetD toprim domains contain the DNA cleavage activity of the Wadjet complex, and this activity is critical for the system’s anti-plasmid defense function.

JetD interactions with JetABC

In our JetD homodimer structure, the N-terminal DUF3322 domains resemble crossed arms positioned above and occluding the DNA binding cleft (Figure 3B). This conformation explains why isolated JetD shows no DNA binding or cleavage activity on its own but also raises the question as to how JetD is activated within the full JetABCD complex. Because the interaction of JetD with JetABC was not stable enough for structure determination by cryoEM, we turned to cross-linking mass spectrometry (XLMS) to identify interacting regions of these subunits. We used XLMS with an isotope-labeled BS³ crosslinker, which crosslinks pairs of lysine side-chains within ~30 Å (C α -C α distance) of one another in native complexes (Herzog et al., 2012). Because the addition of ATP (or a non-hydrolyzable analog) and DNA tended to result in precipitation of the complex over the course of the experiment, we performed these experiments without added nucleotides or DNA. We identified a total of 187 intra- and inter-subunit crosslinks in the JetABCD complex, including 17 crosslinks between JetD and residues in JetA, JetB, and JetC (Figure 5A-B, S9, Table 1).

Since our crosslinking analysis was performed on the Wadjet complex in its Apo state, we modeled an intact JetABC complex in this state (Figure 5C). Starting with our structure of JetA-JetB-JetC^{head}, we modeled the JetC proximal coiled-coils based on our structure of full-length JetABC, and modeled the position of a κ -JetC subunit and associated JetA C-WHD based on a structure of MukBEF in the Apo state (Bürmann et al., 2021). We mapped JetD crosslinks onto this model (Figure 5C) and also onto unclamped JetABC complex structure (Figure 5D) and a model of the “clamped” JetABC complex generated from a structure of bacterial MukBEF in the clamped conformation (Figure 5E) (Bürmann et al., 2021). These models show that JetD crosslinks to residues in the JetC proximal coiled-coils near the ATPase heads, and to nearby residues in both JetA and JetB. On JetD, most JetA/B/C-interacting residues are on the N-terminal Arm and CAP domains, with only a single crosslink detected to a residue in the toprim domain (Figure 5A-B). Overall, these data support a model in which JetD is flexibly tethered via its N-terminal domains near the proximal coiled-coils of JetC, above the clamped DNA, and near where a second DNA may thread through the complex between the JetC coiled-coils (the “ring” DNA).

The KITE subunit JetB possesses a ~50 amino acid unstructured N-terminal tail, which in our clamped JetABC model is located near JetD-interacting residues on the JetC heads and proximal coiled-coils (Figure 5E). In MukBEF, the equivalent region of MukE binds the sequence-specific MukBEF unloader protein MatP and positions this protein between the MukB proximal coiled-coils (Bürmann et al., 2021). We inspected the N-terminus of JetB and identified a highly conserved IFDR motif spanning residues 4-7 of JetB (Figure 6A). To test the role of this motif in complex assembly, we used size-exclusion chromatography to test the association of JetD with either full-length JetAB or a complex lacking the N-terminal 13 residues of JetB (JetAB^{N13}). We found that while full-length JetAB robustly binds JetD, this interaction is completely lost upon deletion of the JetB N-terminus (Figure 6B). We next tested a series of truncations and mutations of JetB, and found that deletion of as few as five N-terminal residues, or mutation of the conserved IFDR motif, is sufficient to eliminate JetD binding (Figure 6A, S10A-B). Further, when we fused the N-terminal 10 residues of JetB to glutathione S-transferase, the fusion protein robustly bound JetD (Figure S10C).

To better understand the molecular basis for JetB-JetD binding, we used AlphaFold2 to model a complex between the two proteins. When provided with the full-length sequences of both proteins, AlphaFold2 consistently generated high-confidence models with the IFDR motif of JetB docked on a hydrophobic surface in the Arm domain of JetD’s N-terminal region (Figure S10D). In these models, the hydrophobic JetB residues 14, F5, and 18 dock directly against a hydrophobic surface on JetD (Figure S10E), while D6 and R7 form hydrogen-bonding interactions with positively and negatively charged surface residues, respectively, on JetD (Figure S10F). This model is consistent with our biochemical data showing that truncation or mutation of the IFDR motif in JetB eliminates JetD binding. We were unable to purify soluble mutants of JetD that altered the putative JetB interaction surface, hampering our ability to directly test the accuracy of this model. Nonetheless, both the modeling and JetB-JetD binding data are consistent with a key role for the JetB N-terminal tail in JetD recruitment and positioning for DNA cleavage.

We next tested whether plasmid cleavage by JetABCD requires the interaction between the JetB N-terminal tail and JetD. We found that truncation of the JetB N-terminus significantly reduces, but does not eliminate, the ability of JetABCD to cleave plasmid DNA (Figure 6C). Thus, while the JetB N-terminal tail is important for JetD recruitment and nuclease activity, it is not absolutely required, suggesting the existence of multiple JetD binding interfaces in the complex. Some JetB proteins including that of *Bacillus cereus* Q1 entirely lack the disordered N-terminal tail (Figure S10G), indicating that additional JetD-binding interfaces must exist in these complexes. Overall, these data strongly implicate JetB in JetD recruitment and/or activation, and support a model in which JetD is flexibly linked to JetABC and positioned near both the “clamped” DNA and the putative second “ring” DNA held between the JetC coiled-coils.

DISCUSSION

Here, we describe the architecture and molecular mechanisms of the bacterial Wadjet defense system, which combines an ATP-powered chemo-mechanical SMC motor and a novel homodimeric DNA endonuclease to specifically recognize and cleave closed-circular plasmid DNA. Thus, rather than using methylation state or sequence-based self/non-self DNA recognition, Wadjet directly senses DNA topology to recognize and destroy foreign DNA. We propose that Wadjet binds DNA and processively extrudes a DNA loop similar to the proposed mechanisms for MukBEF and eukaryotic SMC complexes (Figure 7). In eukaryotic SMC complexes like cohesin and condensin, one DNA segment is stably bound by the HEAT repeat kleisin subunit, and a second is bound by the SMC heads and a second HEAT repeat subunit (Lee et al., 2022; Shaltiel et al., 2022; Shi et al., 2020). Cycles of ATP binding, hydrolysis, and release are postulated to mediate extrusion of a DNA loop between these two sites, through conformational changes in the SMC heads and coiled-coil domains (Kim et al., 2019; Shaltiel et al., 2022). MukBEF and Wadjet contain a single identified DNA binding site at the SMC heads, but in these enzymes dimerization of the complex may enable loop extrusion in a manner similar to eukaryotic cohesin and condensin. Notably, the eukaryotic Smc5/6 complex, which possesses the KITE subunits Nse1 and Nse3 instead of HEAT repeat subunits, was recently shown to extrude DNA loops as a dimeric complex (Pradhan et al., 2022). Thus, formation of dimeric complexes is common among KITE-containing SMC complexes and may play a direct role in DNA loop extrusion.

Our structure of the full-length JetABC complex bears strong resemblance to that of MukBEF, with DNA bound almost identically in the two complexes on the top surface of the dimerized SMC subunit (JetC and MukB) head domains. The major observed difference is in the conformation of the two complexes: while MukBEF adopts a “clamped” state with the MukF dimer bound across the top of the bound DNA to clamp it in place on the MukB heads, JetABC forms an “unclamped” state (Figure 7A-B). In this state, JetA and the associated JetB KITE dimer are rotated $\sim 90^\circ$ downward away from the bound DNA compared to the position of MukEF in the MukBEF complex. The biological significance of the unclamped state is unknown: it may represent a resting state for the complex, or it may represent a structural state in the DNA translocation/loop extrusion cycle.

Processive loop extrusion by the Wadjet complex on a closed-circular DNA substrate would eventually be halted once the entire length of the plasmid has been extruded. We propose that the resulting stalled or “stuck” state of the JetABC complex causes a conformational change that results in recruitment and/or activation of an associated JetD dimer, causing DNA cleavage and release of the Wadjet complex from DNA (Figure 7C). Given the location and flexible nature of JetD’s association with the JetABC complex, we cannot speculate as to whether JetD cleaves DNA bound to the “clamp” site on the JetC dimer heads, or a putative “ring” DNA held between the JetC coiled-coils. Our data showing that Wadjet cleaves different-sized plasmids at equivalent (and very slow, at ~0.01 cleavage events per minute) rates suggests that the DNA loop extrusion step is rapid compared to JetD recruitment and/or activation. We speculate that the rate-limiting step may be opening of the JetD dimer to expose its DNA binding and cleavage sites, and that this opening may be aided by conformational changes in JetABC in the “stuck” state.

The above model can explain Wadjet’s inactivity on linear DNA substrates *in vitro*, and may provide a means for the complex to avoid cleaving the circular bacterial chromosome. On a linear DNA substrate, Wadjet likely binds and extrudes a loop past the ends of the bound DNA, resulting in release of DNA without forming the “stuck” state needed to activate JetD’s nuclease activity. Bacterial chromosomes, meanwhile, are closed-circular DNA molecules but are typically organized into macrodomains and further divided into topologically isolated supercoil domains, which in *E. coli* are ~10 kb in size – similar to the size of a typical plasmid (Badrinarayanan et al., 2015). We propose that Wadjet can bind chromosomal DNA and extrude loops, but given that supercoil domains are isolated by protein binding and plectonemic supercoiling rather than by a direct DNA link, the “stuck” state required for JetD activation may not be adopted during loop extrusion of a chromosomal supercoil domain. Alternatively, given our finding that Wadjet’s catalytic activity is very slow *in vitro*, the complex may cleave chromosomal DNA, but slowly enough that the cell’s DNA repair machinery can efficiently repair these breaks without a significant fitness cost. Further work will be required to distinguish between these models and elucidate the physical mechanisms of nuclease activation in Wadjet, to determine how this complex discriminates between foreign plasmids and its host chromosome.

While the majority of Wadjet systems and related *eptABCD* and *mksBEFG* systems encode all four genes, a sizable minority have lost the nuclease subunit (*JetD/eptD/mksG*), resulting in a variant SMC complex without the ability to cleave plasmid DNA or protect its host from plasmid transformation (Doron et al., 2018; Petrushenko et al., 2011). The best-studied example of such a three-gene system is *Pseudomonas aeruginosa* MksBEF, which has been implicated in chromosome organization and segregation in cooperation with a second bacterial condensin complex, SMC-ScpAB (Lioy et al., 2020; Petrushenko et al., 2011; Zhao et al., 2020). In strains harboring both MksBEF and SMC-ScpAB, the two complexes apparently play distinct roles in chromosome organization (Lioy et al., 2020; Zhao et al., 2020). These distinct roles are likely based on the differing dynamics of the complexes, which potentially involve distinct step sizes, processivity, and specific binding to particular chromosomal regions. This functional specialization of SMC complexes in bacteria resembles the case in eukaryotes, which possess related but distinct condensin I, condensin II, and cohesin complexes with different roles in chromosome organization and

segregation during the more complex eukaryotic cell cycle (Davidson and Peters, 2021; Yatskevich et al., 2019). Furthermore, SMC protein complexes have also been reported to play defensive and maintenance roles in eukaryotes, including the inhibition of viral transcription by the SMC5/6 complex, and the sensing of cytoplasmic DNA by Rad50-CARD9 to trigger an immune response (Aragon, 2018; Roth et al., 2014).

Recent bioinformatics analyses of tens of thousands of bacterial genomes have revealed dozens of confirmed and putative defense systems in bacteria (Doron et al., 2018; Gao et al., 2020). A comparative genomics study suggests that several of these defense systems including the Wadjet system are distributed by transposon-mediated horizontal gene transfer (Benler et al., 2021). While the majority of these systems use enzymes that indiscriminately destroy metabolites, proteins, lipids, or nucleic acids, a few systems encode proteins more typically associated with chromosomal/DNA maintenance or repair, rather than destruction. These include the *hhe* system which incorporates a predicted helicase, *mzaABCDE* which incorporates a protein similar to the mismatch repair protein MutL, and a large number of uncharacterized systems with predicted helicase, SMC ATPase, recombination, and mismatch repair-related proteins (Gao et al., 2020). Notably, these include two recently-identified anti-plasmid defense systems in *Vibrio cholerae*, DdmABC and DdmDE, one subunit of which possesses homology to SMC ATPases (Jaskólska et al., 2022). Thus, in addition to Wadjet, there likely exists a variety of bacterial defense systems that have co-opted DNA maintenance and repair enzymes for the recognition and destruction of foreign DNAs. As with restriction-modification and CRISPR-Cas systems, the unique properties of Wadjet and other chromosome-maintenance related defense systems may also prove useful for new molecular biology or genome-engineering tools.

LIMITATIONS OF THE STUDY

Our structural data on JetABC and JetD reveal a single conformation of these complexes, which is insufficient to fully model or explain the observed biochemical activities of Wadjet. In particular, the structure of JetD reveals an inactive closed state, and we are so far unable to directly measure DNA binding by JetD or visualize its putative open state that binds and cleaves DNA. For JetABC, the observed unclamped state may represent a resting state for the complex, a structural state adopted during the DNA translocation/loop extrusion cycle, or a low-energy state that results from the complex's inability to hydrolyze ATP due to the E1022Q Walker B mutation. Finally, the apparent flexibility of JetD's interaction with JetABC limits our ability to model the structure of the full JetABCD complex, or predict which DNA (that bound to the "clamp" or the putative "ring" site) is cleaved by JetD. Future structural work on the full JetABCD complex bound to closed-circular DNA will be required to answer these remaining questions.

STAR METHODS

RESOURCE AVAILABILITY

Lead contact—Further information and requests for resources and reagents should be directed to and will be fulfilled by the lead contact, Kevin D. Corbett (kcorbett@ucsd.edu).

Materials availability—All unique reagents generated in this study are available from the lead contact with a completed Materials Transfer Agreement.

Data and Code Availability

- The *P. aeruginosa* PA14 JetA-JetB-JetC^{head} cryoEM reconstruction has been deposited at the Electron Microscopy Data Bank (EMDB; <https://www.ebi.ac.uk/emdb/>) under accession number EMD-27480. Corresponding coordinates have been deposited at the RCSB Protein Data Bank (<http://www.rcsb.org>) under accession number 8DK1. The *P. aeruginosa* PA14 JetABC full-length cryoEM reconstruction has been deposited at the Electron Microscopy Data Bank (EMDB; <https://www.ebi.ac.uk/emdb/>) under accession number EMD-27481. Corresponding coordinates have been deposited at the RCSB Protein Data Bank (<http://www.rcsb.org>) under accession number 8DK2. The *P. aeruginosa* PA14 JetC:JetA^{C-WHD} cryoEM reconstruction has been deposited at the Electron Microscopy Data Bank (EMDB; <https://www.ebi.ac.uk/emdb/>) under accession number EMD-27482. Corresponding coordinates have been deposited at the RCSB Protein Data Bank (<http://www.rcsb.org>) under accession number 8DK3. The *P. aeruginosa* PA14 JetD cryoEM reconstruction has been deposited at the Electron Microscopy Data Bank (EMDB; <https://www.ebi.ac.uk/emdb/>) under accession number EMD-25913. Corresponding coordinates have been deposited at the RCSB Protein Data Bank (<http://www.rcsb.org>) under accession number 7TIL. Raw XLMS data for the *P. aeruginosa* PA14 JetABCD complex has been deposited at the PRIDE database (<https://www.ebi.ac.uk/pride/>) under accession number PXD031096. The raw data (uncropped gel images) are available at Mendeley repository <http://dx.doi.org/10.17632/x9923grfjw.1>
- This paper does not report original code.
- Any additional information required to reanalyze the data reported in this paper is available from the lead contact upon request

EXPERIMENTAL MODEL AND SUBJECT DETAILS

All proteins were produced in *E. coli* strain Rosetta2 pLysS (EMD Millipore). Cells were grown in standard media (2XYT broth) with appropriate antibiotics, and standard temperatures (37°C for growth, 20°C for protein expression induction). For plasmid transformation efficiency assays *B. subtilis* BEST7003 derivative strains (generated in this study) were used with appropriate antibiotics.

METHOD DETAILS

Protein expression and purification—All protein sequences used in this study are listed in Table S1. For the expression and purification of proteins, *jetA*, *jetB*, *jetC*, and *jetD* genes from *Pseudomonas aeruginosa* PA14 were cloned into UC Berkeley Macrolab vectors 2-BT and 2-AT (Addgene #29666 and #29665, respectively) for N-terminal TEV protease-cleavable His₆-tag and tagless constructs, respectively. For the co-expression and co-purification of JetAB and their mutants, the genes were amplified and assembled from cloned tagless constructs and reinserted into the 2-BT vector so that JetA is His₆-tagged

and JetB is untagged. PCR-based site-directed mutagenesis was used to generate point mutants. Overlapping PCR followed by isothermal assembly were performed to generate the JetC^{head} construct (JetC^{E1022Q,L783A} 1-284-[SGSSGSSGSS]-781-1101) and the JetB-N10-GST fusion construct. All protein complexes were assembled from separately purified JetAB (N-terminal His₆-tag on JetA), JetC (N-terminal His₆-tagged), and JetD (N-terminal His₆-tag). His₆-tags were not cleaved prior to structural analysis. Of note, tagless JetC showed specific binding with Ni²⁺ affinity columns and the tagless form of JetC was used for biochemical and XLMS experiments.

Proteins were expressed in *E. coli* Rosetta2 pLysS (EMD Millipore) by growing cells to OD₆₀₀=0.6-0.8 followed by induction with 0.33 mM IPTG. The cells were grown at 20°C for 16-18 hours, harvested by centrifugation, and resuspended in ice-cold resuspension buffer (50 mM Tris-HCl pH 7.5, 300 mM NaCl, 10 mM imidazole, 10% Glycerol, 2 mM β-mercaptoethanol). Resuspended cells were lysed using a sonicator followed by lysate clarification using centrifugation. The proteins were purified using Ni²⁺ affinity chromatography (HisTrap HP, Cytiva). Eluted protein was buffer-exchanged into a low salt buffer (20 mM Tris-HCl pH 8.5, 50 mM NaCl, 2 mM β-mercaptoethanol) and subjected for further purification by anion-exchange chromatography (HiTrap Q HP, Cytiva) with a 50 mM to 1 M NaCl gradient. Peak fractions were analyzed by SDS-PAGE, and pure fractions were pooled, concentrated, and separated by size-exclusion chromatography (Superose 6 Increase 10/300 GL, Cytiva) in SEC buffer (20 mM Tris-HCl pH 7.5, 250 mM NaCl, 2 mM β-mercaptoethanol). Peak fractions were pooled, concentrated, and stored at 4°C for biophysical, and biochemical activity assays.

DNA cleavage activity—To measure the DNase activity of Wadjet, 500 ng of pUC18 plasmid DNA was used as a supercoiled DNA form (purified plasmid), linear DNA form (pre-treated with NdeI, New England Biolabs), and relaxed circular DNA form (pre-treated with *E. coli* DNA Topoisomerase I or Nt.BsmAI nicking enzyme, New England Biolabs). 20 μL reactions were performed in the reaction buffer (50 mM HEPES pH 7.5, 20 mM KCl, 1 mM DTT, plus 10 mM MgCl₂ and 2 mM ATP unless otherwise noted). Assays were performed at 37°C for 1 hour and stopped with the addition of 1% SDS and 1X purple gel loading dye (New England Biolabs). Reaction products were resolved on 1% agarose gel in 0.5X TBE buffer at 4°C. The gel was stained with ethidium bromide and imaged on a Bio-Rad Gel Doc system.

To determine the rate of plasmid DNA cleavage and analyze the difference associated with substrate length, pUC1057 (1057 bp, based on an earlier minimization of pUC18 (Staal et al., 2019) incorporating the pUC18 origin of replication with a bleomycin resistance marker) and 2-AT-*jetC* (~8 kb) plasmids were used. Final reactions contained 19.75 nM plasmid and 75 nM of JetA₂B₄C₄D₂ complex with the final buffer composition as 50 mM HEPES pH 7.5, 20 mM KCl, 1 mM DTT, plus 10 mM MgCl₂ and 1 mM ATP. Samples were incubated for 1, 2, 4, 8, and 16 minutes and the reactions were stopped with the addition of 6X purple loading dye (with SDS) and 50 mM EDTA (final concentration). The reactions were resolved on 0.8 % agarose in 1X TAE buffer and the resolved samples were visualized through ethidium bromide staining and imaging on a Bio-Rad Gel Doc system. The substrate (supercoiled and nicked DNA) and product (linear DNA) were quantified

using Fiji/ImageJ (Schindelin et al., 2012) and the fraction linear products were plotted against time in Graphpad Prism.

To determine cleavage site specificity, pUC1057 was treated with Wadjet, separated on a 1% agarose gel, then the linear band was gel-extracted and treated with T4 DNA Polymerase (New England Biolabs) to blunt the ends, then treated with T4 polynucleotide kinase (New England Biolabs). Separately, UC Berkeley Macrolab vector 13S-A (Addgene #48323) was cleaved with EcoRV (New England Biolabs) and treated with calf intestinal phosphatase (New England Biolabs). Wadjet-cleaved and blunted pUC1057 was cloned into 13S-A by blunt-end ligation with T4 DNA ligase (New England Biolabs) at 16°C overnight, then transformed into *E. coli* and plated. Colonies were screened by PCR, then subjected to full-plasmid sequencing (Primordium Labs) to determine cleavage site.

Genome integration of Wadjet operon and mutant variants—*Bacillus subtilis* BEST7003 strain was used as a surrogate host for the *Bacillus cereus* Q1 Wadjet system. The plasmid constructs, pSG1-rfp and pSG1-Wadjet, were obtained from Rotem Sorek. The pSG1-Wadjet vector encodes the full *B. cereus* Q1 Wadjet system with 169 bp upstream and 414 bp downstream sequence, plus a spectinomycin resistance marker and sequences for genomic integration into the *amyE* locus (Doron et al., 2018). Wadjet: *jetC* and Wadjet: *jetD* variants were constructed by introducing stop codon mutations in the open reading frames of their respective genes. *B. subtilis* BEST7003 was transformed as described below, using 200 ng of pSG1 vector DNA. Spectinomycin-resistant transformants were screened on 100 µg/ml spectinomycin containing LB agar plates at 37°C followed by confirmation through colony PCR using gene-specific primers.

Plasmid transformation efficiency—Plasmid transformations were performed following the method from Doron et al. (Doron et al., 2018). To perform plasmid transformation in *B. subtilis* strains, a single colony was inoculated in LB medium and grown overnight at 37°C. Next day, the optical density for the cultures from various strains was measured and normalized for equal bacterial cell density with dilution in LB. 10 µL of normalized density culture was diluted into 1 mL of MC medium (80 mM K₂HPO₄, 30 mM KH₂PO₄, 2% glucose, 30 mM trisodium citrate, 22 µg/ml ferric ammonium citrate, 0.1% casein hydrolysate (CAA), 0.2% potassium glutamate) supplemented with 10 mM MgSO₄ and grown for 3 hours at 37°C. 250 ng of the chloramphenicol-resistant episomal shuttle plasmid pBS42 (Bacillus Genetic Stock Center ID: ECE10) was mixed with 300 µL of cells (in a 15 mL culture tube), incubated for 3 hours at 37°C with agitation. Parts of the transformed culture were plated on LB agar plates containing 100 µg/mL spectinomycin plus 5 µg/mL chloramphenicol and plates containing only 100 µg/mL spectinomycin. The relative plasmid transformation efficiency was plotted and shown are the results from three technical replicates plotted as average plus or minus standard deviation.

ATPase activity measurement—ATP hydrolysis was measured using ADP-Glo Kinase assay kit (Promega) following the protocol provided by the manufacturer. In brief, the reactions were performed (as mentioned above) with the exception that 50 µM of ultra-pure ATP, and 400 nM of protein or complexes were used in a final reaction as 5 µL volume. The 45 min reaction incubation at 37°C was followed by addition of ADP Glo reagent and

finally kinase detection reagents (Promega). The luminescence was measured in a 384-well plate using the TECAN (Mannedorf, Switzerland) Infinite M1000 microplate reader. The standard curve was calculated using a known concentration mixture of ADP and ATP. The measurements are shown as a mean of four technical replicates with standard deviation.

Protein interaction assays and oligomeric state determination—For the interaction analysis of various proteins, SEC using the Superose 6 Increase 10/300 GL column was employed. The proteins (or pre-formed JetAB complex) were mixed (concentrations ranging from 5-20 μM) and incubated on ice for 20-30 minutes prior to injection into the SEC column. The fractions corresponding to the range of peaks were analyzed on SDS-PAGE and the interactions were determined with changes in the retention time.

For analysis of oligomeric states by size-exclusion chromatography coupled to multi-angle light scattering (SEC-MALS), a 100 μL protein sample at 2 mg/mL was passed over a Superose 6 Increase 10/300 GL column (Cytiva) in SEC buffer. Light scattering and refractive index profiles were collected by miniDAWN TREOS and Optilab T-rEX detectors (Wyatt Technology), respectively, and molecular weight was calculated using ASTRA v.8 software (Wyatt Technology).

Cryoelectron microscopy sample preparation and data acquisition—For cryoEM grid preparation of the JetA-JetB-JetC^{head} complex, separately expressed JetAB and JetC^{head} were mixed to give a final ratio of 2 JetA:4 JetB:4 JetC in TNT buffer (20 mM Tris-HCl pH7.5, 200 mM NaCl, 1 mM TCEP, and 2 mM MgCl₂) and incubated on ice for 10 min. The incubated samples were mixed with 5 μM of annealed 65 bp dsDNA (JetABC_cryo_Fwd and JetABC_cryo_Rev; Key Resources Table) and 5 mM ATP- γ -S followed by 10 min incubation on ice. The samples were further passed through Zeba Spin Desalting Columns (7K MWCO) (Thermo Fisher Scientific) which were pre-equilibrated with JetABC-EM buffer (30 mM Tris-HCl pH 7.5, 60 mM NaCl, 1 mM TCEP, and 2 mM MgCl₂. 1 mM ATP- γ -S) plus 0.05% (w/v) β -octyl glucoside). Immediately prior to use, Quantifoil copper 1.2/1.3 300 mesh grids were plasma cleaned for 10 sec in a pre-set program using a Solarus II plasma cleaner (Gatan). Protein sample (4 μM as a 2:4:4 complex) was applied to the grid as a 3.5 μL drop in the environmental chamber of a Vitrobot Mark IV (Thermo Fisher Scientific) held at 4°C and 100% humidity. After brief incubation, the grid was blotted with filter paper for 5 seconds followed by plunging into liquid ethane cooled by liquid nitrogen. Grids were mounted into standard AutoGrids (Thermo Fisher Scientific) for imaging. The sample was imaged using a Titan Krios G3 transmission electron microscope (Thermo Fisher Scientific) operated at 300 kV configured for fringe-free illumination and equipped with a K2 direct electron detector (Gatan) mounted post Quantum 968 LS imaging filter (Gatan). The microscope was operated in EFTEM mode with a slit-width of 20 eV and using a 100 μm objective aperture. Automated data acquisition was performed using EPU (Thermo Fisher Scientific) and all images were collected using the K2 in counting mode. Ten-second movies were collected at a magnification of 165,000x and a pixel size of 0.84 Å, with a total dose of 54.1 e⁻/Å² distributed uniformly over 40 frames. In total, 1280 movies were acquired with a realized

defocus range of -0.5 to -2.5 μm . 1132 out of 1280 images were used for final analysis after excluding micrographs based on poor CTF fitting, excessive motion, or thick ice.

For cryoEM grid preparation of the JetA+JetB+JetC+DNA complex, separately expressed JetAB and JetC^{E1022Q} were mixed to give a final ratio of 2 JetA:4 JetB:4 JetC following the procedure above for JetA-JetB-JetC^{head} complex sample preparation. Immediately prior to use, Quantifoil copper 1.2/1.3 300 mesh grids were plasma cleaned for 12 sec in a pre-set program using a Solarus II plasma cleaner (Gatan). Protein sample (3 μM as a 2:4:4 complex) was applied to the grid as a 3.5 μL drop in the environmental chamber of a Vitrobot Mark IV (Thermo Fisher Scientific) held at 4°C and 100% humidity. After brief incubation, the grid was blotted with filter paper for 5 seconds followed by plunging into liquid ethane cooled by liquid nitrogen. Grids were mounted into standard AutoGrids (Thermo Fisher Scientific) for imaging. The sample was imaged using a Titan Krios G3 transmission electron microscope (Thermo Fisher Scientific) operated at 300 kV configured for fringe-free illumination and equipped with a K2 direct electron detector (Gatan) mounted post Quantum 968 LS imaging filter (Gatan). The microscope was operated in EFTEM mode with a slit-width of 20 eV and using a 100 μm objective aperture. Automated data acquisition was performed using EPU (Thermo Fisher Scientific) and all images were collected using the K2 in counting mode. Ten-second movies were collected at a magnification of 130,000x and a pixel size of 1.10 \AA , with a total dose of 50.1 $\text{e}^-/\text{\AA}^2$ distributed uniformly over 40 frames. In total, 3094 movies were acquired with a realized defocus range of -0.5 to -2.5 μm . 3049 out of 3094 images were used for final analysis after excluding micrographs based on poor CTF fitting, excessive motion, or thick ice.

For cryoEM grid preparation of JetD, protein (with N-terminal TEV cleavable His₆ tag) was purified to homogeneity using a size-exclusion chromatography in JetD EM buffer (20 mM Tris pH 7.5, 200 mM NaCl, 2 mM β -mercaptoethanol). Immediately prior to use, UltrAufoil 1.2/1.3 300 mesh grids were plasma cleaned for 12 sec in a pre-set program using a Solarus II plasma cleaner (Gatan). Protein sample (13 μM as a dimer) was applied to the grid as a 3.5 μL drop in the environmental chamber of a Vitrobot Mark IV (Thermo Fisher Scientific) held at 4°C and 100% humidity. After 1 minute of incubation, the grid was blotted with filter paper for 5 seconds followed by plunging into liquid ethane cooled by liquid nitrogen. Grids were mounted into standard AutoGrids (Thermo Fisher Scientific) for imaging. The sample was imaged using a Titan Krios G3 transmission electron microscope (Thermo Fisher Scientific) operated at 300 kV configured for fringe-free illumination and equipped with a K2 direct electron detector (Gatan) mounted post Quantum 968 LS imaging filter (Gatan). The microscope was operated in EFTEM mode with a slit-width of 20 eV and using a 100 μm objective aperture. Automated data acquisition was performed using EPU (Thermo Fisher Scientific) and all images were collected using the K2 in counting mode. Ten-second movies were collected at a magnification of 215,000x and a pixel size of 0.65 \AA , with a total dose of 62 $\text{e}^-/\text{\AA}^2$ distributed uniformly over 40 frames. In total, 1225 movies were acquired with a realized defocus range of -0.5 to -2.5 μm . 1175 out of 1225 images were used for final analysis after excluding micrographs based on poor CTF fitting, excessive motion, or thick ice.

Cryoelectron microscopy data processing—CryoEM data analysis was performed in cryoSPARC version 3.2 (Punjani et al., 2017) (Figures S3, S5, S8, Table 1). Movies were motion-corrected using patch motion correction (multi) and CTF-estimated using patch CTF estimation (multi) (Zheng et al., 2017). For analysis of the JetA-JetB-JetC^{head} complex (Figure S3), the blob picker was used for initial particle picking. A 415K particle set was subjected to multiple rounds of 2D and 3D classification in cryoSPARC, resulting in a cleaned particle stack of 131K particles. This particle stack was used for *ab initio* reconstruction and homogenous refinement in cryoSPARC, resulting in a 3.22 Å resolution initial reconstruction. This structure was used to generate templates for template-based particle picking, resulting in a new ~1M particle set. Multiple rounds of 2D and 3D classification, duplicate removal, and manual movie curation resulted in a final cleaned particle stack of 130,904 particles. These particles were re-extracted at full resolution and used for *ab initio* reconstruction and non-uniform refinement with C2 symmetry applied, yielding a final resolution of 2.95 Å. Initial models for JetA, JetB, and JetC were generated by AlphaFold2 (Jumper et al., 2021). These models were manually docked into sharpened maps (performed using DeepEMhancer (Sanchez-Garcia et al., 2021)) using UCSF Chimera (Pettersen et al., 2004), manually rebuilt in COOT (Emsley et al., 2010), and subjected to real-space refinement in phenix.refine (Afonine et al., 2018).

For analysis of the JetA+JetB+JetC+DNA complex (Figure S5), the circular blob picker was used for initial particle picking. A 3M particle set was subjected to multiple rounds of 2D and 3D classification in cryoSPARC, resulting in a cleaned particle stack of 325K particles that contain at least a dimer of JetC and bound DNA. This particle stack was re-extracted at full resolution and used for *ab initio* reconstruction and refinement in cryoSPARC, resulting in a 3.28 Å resolution reconstruction of the DNA-bound JetC dimer head. Next, the same 325K particles were re-centered on the JetC coiled-coils and re-extracted using bigger boxes, then subjected to further 2D classifications and heterogeneous refinements, and 3D classification followed by homogenous refinement. A 36K particle set representing a JetA₂B₄C₂ complex was subjected to homogenous refinement, resulting in a 4.5 Å initial structure that was used for template-based particle picking.

Next, both elliptical blob picking (1.6M particles) and template-based picking (987K particles) were used, and the resulting particle stacks separately subjected to 2D classification. A final particle set was assembled by combining 172K particles from circular blob picking, 246K particles from elliptical blob picking, and 300K particles from template picking, which resulted in a final particle stack of 297K particles after heterogeneous refinement and duplicate removal. 3D classification focused on the JetC coiled-coil elbow resulted in a 177K particle set that was refined to produce a 3.8 Å resolution structure of the JetC dimer. Separate 3D classification focused on JetAB resulted in a 57K particle set that was refined to produce a 4.1 Å resolution structure of the JetA₂B₄C₂ complex.

To build the full model of JetA₂B₄C₂, refined models for JetA, JetB, and the JetC head from our JetA-JetB-JetC^{head} structure were manually docked into sharpened maps (performed using DeepEMhancer (Sanchez-Garcia et al., 2021)) using UCSF Chimera (Pettersen et al., 2004). An AlphaFold2 model of the JetC proximal coiled-coil was manually docked and then refined using ISOLDE (Croll, 2018) as a plugin for UCSF ChimeraX (Pettersen et

al., 2021). The final models were manually rebuilt in COOT and the DNA was modeled as polyAT dsDNA helix (Emsley et al., 2010), and subjected to real-space refinement in phenix.refine, using protein secondary structure and DNA base pairing, stacking, and planarity restraints (Afonine et al., 2018).

For analysis of JetD (Figure S8), the blob picker was used for initial particle picking. A ~1.9M particle set was subjected to multiple rounds of 2D and 3D classification, resulting in a final cleaned particle stack of 37,757 particles. A subset of these particles (20,991) were used to train the Topaz particle picker (Bepler et al., 2019), which picked a separate set of ~573K particles. These particles were subjected to multiple rounds of 2D and 3D classification, resulting in a final cleaned particle stack of 47,962 particles. The blob-picked and Topaz-picked particle sets were combined, re-extracted at full resolution, and duplicates were removed, resulting in a final particle set of 64,260 particles. This particle set was used for ab initio reconstruction and heterogeneous refinement, with 51,336 particles segregating to one model. This model was refined using non-uniform refinement in cryoSPARC, yielding a final resolution of 3.69 Å. Two separate local refinement jobs were performed with masks isolating either the N-terminal DUF3322 domain dimer (final resolution 3.45 Å) or the C-terminal toprim domain dimer (final resolution 3.61 Å).

An initial model for JetD was generated by AlphaFold2 (Jumper et al., 2021). The N- and C-terminal domains of this model were manually docked into sharpened maps (sharpening performed using DeepEMhancer (Sanchez-Garcia et al., 2021)) using UCSF Chimera (Pettersen et al., 2004), and then manually rebuilt in COOT (Emsley et al., 2010). Separate models for the DUF3322 domain dimer and toprim domain dimer were built into local refinement maps and real-space refined against unsharpened maps in phenix.refine (Afonine et al., 2018), using secondary structure restraints. Additionally, NCS restraints were used in the modeling of the DUF3322 domain dimer. These models were manually docked into the overall map, the inter-domain linker manually rebuilt, then real-space refined with reference model restraints for both domains. Structures were visualized in ChimeraX (Pettersen et al., 2021).

Cross-linking Mass spectrometry—JetAB, JetC, and JetD proteins were purified as discussed above. JetABCD complex was reconstituted *in vitro* and purified through SEC in the cross-linking buffer (20 mM HEPES pH 7.5, 200 mM NaCl, 1 mM DTT) using Superose 6 Increase 10/300 GL column (Cytiva). Peak fractions corresponding to the reconstituted complexes were pooled and concentrated to 0.5 mg/mL protein concentration. Cross-linking with isotopically labeled BS³-H12/D12 (Creative molecules Inc.) was optimized and performed in a 250 µL reaction with 3.5 mM concentration of the crosslinker. The reaction was allowed to proceed at 37°C for 1 hour with constant shaking of 750 rpm in a thermomixer (Eppendorf). The reaction was quenched with the addition of 50 mM final concentration of ammonium bicarbonate and allowed to incubate at 37°C for another 20 minutes. SDS and Tris(2-carboxyethyl)phosphine (TCEP) were added to the reaction mixture to a final concentration of 1% and 2 mM, respectively, and the mixture was heated for 5 minutes at 100°C. To modify the cysteines, iodoacetamide was added to a 30 mM final concentration, and the reaction was allowed to proceed for the next 30 minutes at room temperature in dark. The crosslinked protein/complex sample was precipitated with

ethanol:acetone:acetic acid (50:49.9:0.1 vol/vol/vol) followed by high-speed centrifugation and three times washing of pellets with 80% ethanol: acetone: acetic acid (50:49.9:0.1). The samples were evaporated to dryness in a SpeedVac concentrator. The dried samples were resuspended in 8 M urea, followed by the dilution of urea to 1 M with 50 mM ammonium bicarbonate buffer. Sequencing-grade trypsin (Promega) was added into the reaction tubes (1:50 to the sample concentration) and protein digestion was allowed to proceed overnight with incubation at 37°C. The next day, reactions were acidified using trifluoroacetic acid, and reaction products were extracted using Sep-Pak C18 cartridges as per the manufacturer's protocol (Waters). The peptides were eluted (in 80% acetonitrile + 0.1 acetic acid) in a silanized vial.

To enrich the concentration of cross-linked peptides, SEC was performed using a Superdex 30 Increase 10/300 GL column (Cytiva) in XL-SEC Buffer (acetonitrile:water:TFA in 30:69.9:0.1 vol/vol/vol). Four fractions corresponding to a volume range of 10-12 mL elution volume were harvested and evaporated to dryness in a SpeedVac concentrator. The samples were resuspended in water. LC-MS/MS analysis was performed using an Orbitrap Fusion Lumos Tribrid mass spectrometer (Thermo Fisher Scientific) coupled in-line with Ultimate 3000 RSLCnano UHPLC (Dionex, Thermo Fisher Scientific). For the sample separation, Mobile phase A (0.1% formic acid) and Mobile phase B (99.9% acetonitrile and 0.1% formic acid) were used with the customized gradient protocol (0-17 min with 0% Mobile phase B, 17-137 min with 6-50% Mobile phase B, 137-140 min with 75% Mobile phase B, 140-150 min with 75% Mobile phase B, followed by 0% Mobile phase B until 165 min) (Dionex, Thermo Fisher Scientific). The sample was ionized using Nanospray Flex (Thermo Fisher Scientific). Approximately 1 µg of sample was injected into a custom packed column (174 cm length, packed with 1 cm of C4 resin (5µ×120Å) and 12 cm of C18 resin (2.2µ×120Å) resuspended in ethanol:acetonitrile:acetic acid mix (in 50:49.9:0.1 vol/vol/vol) at 100psi pressure (Polymorphic Technologies part number 2000023)). The mass spectrometer was operated in data-dependent mode with Orbitrap resolution of 120000 for MS1 with a scan range of 300-1600 m/z. For the MS2 scan, precursor ions with a charge state between +3 to +6 were selected for fragmentation using HCD energy 30% with a resolution of 30000.

Data Analysis and visualization of crosslinked peptides—The mass spectrometry raw files were converted to .MZxml file types using msConvert software (Chambers et al., 2012) with data export settings described by Leitner et al. (Leitner et al., 2014). Decoy sequence was created by reversing the amino acid sequence using SPELLBACKWARDS tool (<http://spellbackwards.com/>). The cross-linking mass spectrometry data was analysed using xQuest.xProphet software using default parameters (Leitner et al., 2014). In addition to K:K, possible cross-linking between K:S, K:T, K:Y were also included. The associated raw data was submitted to the PRIDE database (Perez-Riverol et al., 2022). The crosslinks with FDR values of 0.1 and 0.05 were finally selected to report inter- and intra-subunit crosslinks, respectively. The hits were manually curated to remove the redundant crosslinks from different enriched fractions. An offset of -18 residues numbering (to compensate for TEV cleavable His₆-tag) was applied for JetA and JetD sequences and hits are reported in Table S2. For the visualization of crosslinks, the xVis web server tool was used (Grimm et

al., 2015). The Xlink analyzer plug-in tool was used for the analysis of crosslinks on solved or modeled structures (Kosinski et al., 2015).

Protein structure prediction using AlphaFold2 modeling—For Wadjet structure prediction and modeling, we used AlphaFold2 (Jumper et al., 2021) as implemented by the ColabFold project (Mirdita et al., 2022), including multiple sequence alignment generation using MMseqs2 (Steinegger and Söding, 2017) and model relaxation using the AMBER force field option (Hornak et al., 2006).

Protein sequences are listed in Table S1 and the input parameters and confidence score for the modeling of each protein/complex are given below:

JetC coiled-coil: ColabFold notebook: AlphaFold2, residue range: 246-442-(GSGSG)-611-848, homooligomer: 1, multiple sequence alignment method: mmseqs2, pair mode: unpaired, pLDDT: 88.10.

JetC distal region: ColabFold notebook: AlphaFold2, residue range: 343 to 690, homooligomer: 2, multiple sequence alignment method: mmseqs2, pair mode: unpaired, pLDDT: 93.85, pTM score: 0.75.

JetB + JetD: ColabFold notebook: AlphaFold2_advanced, residue range: 1-249 (JetB); 1-381 (JetD), homooligomer: 1 (JetA); 1 (JetB), multiple sequence alignment method: mmseqs2, pair mode: unpaired, pLDDT: 80.26, pTM score: 0.47.

pUC1057 plasmid information—Sequence features and location:- Origin of replication: 7-595; Bleomycin resistance gene: 620-994; Promoter for bleomycin resistance gene: 995-1

Nucleotide sequence:

```
AAGCTTTTTCCATAGGCTCCGCCCCCTGACGAGCATCACAAAATCGACGCTCA
AGTCAGAGGTGGCGAAACCCGACAGGACTATAAAGATACCAGGCGTTCCCCCTG
GAAGCTCCCTCGTGCGCTCTCCTGTTCCGACCCTGCCGCTTACCGGATACCTGTCC
GCCTTTCTCCCTTCGGGAAGCGTGGCGCTTTCTCATAGCTCACGCTGTAGGTATCT
CAGTTCGGTGTAGGTCGTTTCGCTCCAAGCTGGGCTGTGTGCACGAACCCCCCGTT
CAGCCCGACCGCTGCGCCTTATCCGGTAACTATCGTCTTGAGTCCAACCCGGTAAG
ACACGACTTATCGCCACTGGCAGCAGCCACTGGTAACAGGATTAGCAGAGCGAGG
TATGTAGGCGGTGCTACAGAGTTCTTGAAGTGGTGGCCTAACTACGGCTACACTAG
AAGGACAGTATTTGGTATCTGCGCTCTGCTGAAGCCAGTTACCTTCGGAAAAAGA
GTTGGTAGCTCTTGATCCGGCAAACAAACCACCGCTGGTAGCGGTGGTTTTTTTTG
TTTGCAAGCAGCAGATTACGCGCAGAAAAAAGGATCTCAAGAAGATCCTTTGAT
CTTTTCTACGTCAGTCCTGCTCCTCGCCACGAAGTGCACGCAGTTGCCGGCCGG
GTCGCGCAGGGCGAACTCCCGCCCCACGGCTGCTCGCCGATCTCGGTTCATGGCC
GGCCCGGAGGCGTCCCGGAAGTTCGTGGACACGACCTCCGACCACTCGGCGTAC
AGCTCGTCCAGGCCGCGCACCCACACCCAGGCCAGGGTGTGTCCGGCACACC
TGGTCTGGACCGCGCTGATGAACAGGGTACGTCGTCCCGGACCACACCGGCG
AAGTCGTCCTCCACGAAGTCCCGGGAGAACCCGAGCCGGTCCGTTCCAGAACTCG
ACCGCTCCGGCGACGTCGCGCGCGGTGAGCACCGGAACGGCACTGGTCAACTTG
```

GCCATACTCTTCCTTTTTCAATATTATTGAAGCATTTATCAGGGTTATTGTCTCATGA
GCGGATACAT

QUANTIFICATION AND STATISTICAL ANALYSIS

Quantification of Wadjet cleaved products (related to Figure S2) was performed using Fiji/ImageJ and data fittings and slope calculations were performed in Graphpad Prism.

Supplementary Material

Refer to Web version on PubMed Central for supplementary material.

ACKNOWLEDGEMENTS

The authors thank Rotem Sorek for sharing *Bacillus subtilis* strains and Wadjet system clones, Robert Ashley and Marius Matyszewski for help with cryoelectron microscopy data collection, Frank Bürmann and Jan Löwe for sharing MukBEF model coordinates prior to publication, Amit Kumar Gupta for help with xQuest/xProphet software installation, Arshad Desai and James Berger for critical reading of the manuscript, and the Corbett and Zhou labs for helpful discussions. All electron microscopy data were collected at the UCSD Cryo-EM Facility, which was built and equipped with funds from UCSD and an initial gift from the Agouron Institute, K.D.C. acknowledges funding from the National Institutes of Health R35 GM144121. H.Z. acknowledges funding from the National Institutes of Health R01 GM116897 and S10 OD023498. M.H. acknowledges funding from the National Institutes of Health R35 GM138206.

REFERENCES

- Adusumilli R, and Mallick P (2017). Data Conversion with ProteoWizard msConvert. *Methods Mol Biol* 1550, 339–368. [PubMed: 28188540]
- Afonine PV, Poon BK, Read RJ, Sobolev OV, Terwilliger TC, Urzhumtsev A, and Adams PD (2018). Real-space refinement in PHENIX for cryo-EM and crystallography. *Acta Crystallogr D Struct Biol* 74, 531–544. [PubMed: 29872004]
- Aragón L (2018). The Smc5/6 Complex: New and Old Functions of the Enigmatic Long-Distance Relative. *Annu. Rev. Genet* 52, 89–107. [PubMed: 30476445]
- Aravind L, Leipe DD, and Koonin EV (1998). Toprim—a conserved catalytic domain in type IA and II topoisomerases, DnaG-type primases, OLD family nucleases and RecR proteins. *Nucleic Acids Res.* 26, 4205–4213. [PubMed: 9722641]
- Arber W, and Linn S (1969). DNA modification and restriction. *Annu. Rev. Biochem* 38, 467–500. [PubMed: 4897066]
- Badrinarayanan A, Reyes-Lamothe R, Uphoff S, Leake MC, and Sherratt DJ (2012). In vivo architecture and action of bacterial structural maintenance of chromosome proteins. *Science* 338, 528–531. [PubMed: 23112333]
- Badrinarayanan A, Le TBK, and Laub MT (2015). Bacterial chromosome organization and segregation. *Annu. Rev. Cell Dev. Biol* 31, 171–199. [PubMed: 26566111]
- Benler S, Faure G, Altae-Tran H, Shmakov S, Zheng F, and Koonin E (2021). Cargo Genes of Tn7-Like Transposons Comprise an Enormous Diversity of Defense Systems, Mobile Genetic Elements, and Antibiotic Resistance Genes. *MBio* 12, e0293821. [PubMed: 34872347]
- Bepler T, Morin A, Rapp M, Brasch J, Shapiro L, Noble AJ, and Berger B (2019). Positive-unlabeled convolutional neural networks for particle picking in cryo-electron micrographs. *Nat. Methods* 16, 1153–1160. [PubMed: 31591578]
- Bergerat A, de Massy B, Gadelle D, Varoutas PC, Nicolas A, and Forterre P (1997). An atypical topoisomerase II from Archaea with implications for meiotic recombination. *Nature* 386, 414–417. [PubMed: 9121560]
- Böhm K, Giacomelli G, Schmidt A, Imhof A, Koszul R, Marbouty M, and Bramkamp M (2020). Chromosome organization by a conserved condensin-ParB system in the actinobacterium *Corynebacterium glutamicum*. *Nat. Commun* 11, 1485. [PubMed: 32198399]

- Bürmann F, Funke LFH, Chin JW, and Löwe J (2021). Cryo-EM structure of MukBEF reveals DNA loop entrapment at chromosomal unloading sites. *Mol. Cell* 81, 4891–4906.e8. [PubMed: 34739874]
- Chambers MC, Maclean B, Burke R, Amodei D, Ruderman DL, Neumann S, Gatto L, Fischer B, Pratt B, Egertson J, et al. (2012). A cross-platform toolkit for mass spectrometry and proteomics. *Nat. Biotechnol* 30, 918–920. [PubMed: 23051804]
- Corbett KD, Benedetti P, and Berger JM (2007). Holoenzyme assembly and ATP-mediated conformational dynamics of topoisomerase VI. *Nat. Struct. Mol. Biol* 14, 611–619. [PubMed: 17603498]
- Croll TI (2018). ISOLDE: a physically realistic environment for model building into low-resolution electron-density maps. *Acta Crystallogr D Struct Biol* 74, 519–530. [PubMed: 29872003]
- Danilova O, Reyes-Lamothe R, Pinskaya M, Sherratt D, and Possoz C (2007). MukB colocalizes with the oriC region and is required for organization of the two Escherichia coli chromosome arms into separate cell halves. *Mol. Microbiol* 65, 1485–1492. [PubMed: 17824928]
- Davidson IF, and Peters J-M (2021). Genome folding through loop extrusion by SMC complexes. *Nat. Rev. Mol. Cell Biol* 22, 445–464. [PubMed: 33767413]
- Davidson IF, Bauer B, Goetz D, Tang W, Wutz G, and Peters J-M (2019). DNA loop extrusion by human cohesin. *Science* 366, 1338–1345. [PubMed: 31753851]
- Doron S, Melamed S, Ofir G, Leavitt A, Lopatina A, Keren M, Amitai G, and Sorek R (2018). Systematic discovery of antiphage defense systems in the microbial pangenome. *Science* 359, eaar4120. [PubMed: 29371424]
- Emsley P, Lohkamp B, Scott WG, and Cowtan K (2010). Features and development of Coot. *Acta Crystallogr. D Biol. Crystallogr* 66, 486–501. [PubMed: 20383002]
- Fennell-Fezzie R, Gradia SD, Akey D, and Berger JM (2005). The MukF subunit of Escherichia coli condensin: architecture and functional relationship to kleisins. *EMBO J.* 24, 1921–1930. [PubMed: 15902272]
- Fineran PC, Blower TR, Foulds IJ, Humphreys DP, Lilley KS, and Salmond GPC (2009). The phage abortive infection system, ToxIN, functions as a protein-RNA toxin-antitoxin pair. *Proc. Natl. Acad. Sci. U. S. A* 106, 894–899. [PubMed: 19124776]
- Ganji M, Shaltiel IA, Bisht S, Kim E, Kalichava A, Haering CH, and Dekker C (2018). Real-time imaging of DNA loop extrusion by condensin. *Science* 360, 102–105. [PubMed: 29472443]
- Gao L, Altae-Tran H, Böhning F, Makarova KS, Segel M, Schmid-Burgk JL, Koob J, Wolf YI, Koonin EV, and Zhang F (2020). Diverse enzymatic activities mediate antiviral immunity in prokaryotes. *Science* 369, 1077–1084. [PubMed: 32855333]
- Goloborodko A, Imakaev MV, Marko JF, and Mirny L (2016). Compaction and segregation of sister chromatids via active loop extrusion. *Elife* 5, e148464.
- Graille M, Cladière L, Durand D, Lecointe F, Gabelle D, Quevillon-Cheruel S, Vachette P, Forterre P, and van Tilbeurgh H (2008). Crystal structure of an intact type II DNA topoisomerase: insights into DNA transfer mechanisms. *Structure* 16, 360–370. [PubMed: 18334211]
- Granato ET, Meiller-Legrand TA, and Foster KR (2019). The Evolution and Ecology of Bacterial Warfare. *Curr. Biol* 29, R521–R537. [PubMed: 31163166]
- Grimm M, Zimniak T, Kahraman A, and Herzog F (2015). xVis: a web server for the schematic visualization and interpretation of crosslink-derived spatial restraints. *Nucleic Acids Res.* 43, W362–W369. [PubMed: 25956653]
- Herzog F, Kahraman A, Boehringer D, Mak R, Bracher A, Walzthoeni T, Leitner A, Beck M, Hartl F-U, Ban N, et al. (2012). Structural probing of a protein phosphatase 2A network by chemical cross-linking and mass spectrometry. *Science* 337, 1348–1352. [PubMed: 22984071]
- Hornak V, Abel R, Okur A, Strockbine B, Roitberg A, and Simmerling C (2006). Comparison of multiple Amber force fields and development of improved protein backbone parameters. *Proteins* 65, 712–725. [PubMed: 16981200]
- Jaskólska M, Adams DW, and Blokesch M (2022). Two defence systems eliminate plasmids from seventh pandemic Vibrio cholerae. *Nature* 604, 323–329. [PubMed: 35388218]

- Jumper J, Evans R, Pritzel A, Green T, Figurnov M, Ronneberger O, Tunyasuvunakool K, Bates R, Žídek A, Potapenko A, et al. (2021). Highly accurate protein structure prediction with AlphaFold. *Nature* 596, 583–589. [PubMed: 34265844]
- Kapust RB, Tózsér J, Fox JD, Anderson DE, Cherry S, Copeland TD, and Waugh DS (2001). Tobacco etch virus protease: mechanism of auto lysis and rational design of stable mutants with wild-type catalytic proficiency. *Protein Eng.* 14, 993–1000. [PubMed: 11809930]
- Keeney S, Giroux CN, and Kleckner N (1997). Meiosis-specific DNA double-strand breaks are catalyzed by Spo11, a member of a widely conserved protein family. *Cell* 88, 375–384. [PubMed: 9039264]
- Kim Y, Shi Z, Zhang H, Finkelstein IJ, and Yu H (2019). Human cohesin compacts DNA by loop extrusion. *Science* 366, 1345–1349. [PubMed: 31780627]
- Kosinski J, von Appen A, Ori A, Karius K, Müller CW, and Beck M (2015). Xlink Analyzer: software for analysis and visualization of cross-linking data in the context of three-dimensional structures. *J. Struct. Biol* 189, 177–183. [PubMed: 25661704]
- Lau RK, Ye Q, Birkholz EA, Berg KR, Patel L, Mathews IT, Watrous JD, Ego K, Whiteley AT, Lowey B, et al. (2020). Structure and Mechanism of a Cyclic Trinucleotide-Activated Bacterial Endonuclease Mediating Bacteriophage Immunity. *Mol. Cell* 77, 723–733.e6. [PubMed: 31932164]
- Lee B-G, Rhodes J, and Löwe J (2022). Clamping of DNA shuts the condensin neck gate. *Proc. Natl. Acad. Sci. U. S. A* 119, e2120006119. [PubMed: 35349345]
- Leitner A, Walzthoeni T, and Aebersold R (2014). Lysine-specific chemical cross-linking of protein complexes and identification of cross-linking sites using LC-MS/MS and the xQuest/xProphet software pipeline. *Nat. Protoc* 9, 120–137. [PubMed: 24356771]
- Lioy VS, Cournac A, Marbouty M, Duigou S, Mozziconacci J, Espéli O, Boccard F, and Koszul R (2018). Multiscale Structuring of the *E. coli* Chromosome by Nucleoid-Associated and Condensin Proteins. *Cell* 172, 771–783.e18. [PubMed: 29358050]
- Lioy VS, Junier I, Lagage V, Vallet I, and Boccard F (2020). Distinct Activities of Bacterial Condensins for Chromosome Management in *Pseudomonas aeruginosa*. *Cell Rep.* 33, 108344. [PubMed: 33147461]
- Mäkelä J, and Sherratt D (2020a). SMC complexes organize the bacterial chromosome by lengthwise compaction. *Curr. Genet* 66, 895–899. [PubMed: 32300862]
- Mäkelä J, and Sherratt DJ (2020b). Organization of the *Escherichia coli* Chromosome by a MukBEF Axial Core. *Mol. Cell* 78, 250–260.e5. [PubMed: 32097603]
- Millman A, Bernheim A, Stokar-Avihail A, Fedorenko T, Voicheck M, Leavitt A, Oppenheimer-Shaanan Y, and Sorek R (2020). Bacterial Retrons Function In Anti-Phage Defense. *Cell* 183, 1551–1561.e12. [PubMed: 33157039]
- Millman A, Melamed S, Leavitt A, Doron S, Bernheim A, Hör J, Lopatina A, Ofir G, Hochhauser D, Stokar-Avihail A, et al. (2022). An expanding arsenal of immune systems that protect bacteria from phages.
- Mirdita M, Schütze K, Moriwaki Y, Heo L, Ovchinnikov S, and Steinegger M (2022). ColabFold: making protein folding accessible to all. *Nat. Methods* 19, 679–682. [PubMed: 35637307]
- Nichols MD, DeAngelis K, Keck JL, and Berger JM (1999). Structure and function of an archaeal topoisomerase VI subunit with homology to the meiotic recombination factor Spo11. *EMBO J.* 18, 6177–6188. [PubMed: 10545127]
- Niki H, Jaffé A, Imamura R, Ogura T, and Hiraga S (1991). The new gene mukB codes for a 177 kd protein with coiled-coil domains involved in chromosome partitioning of *E. coli*. *EMBO J.* 10, 183–193. [PubMed: 1989883]
- Panas MW, Jain P, Yang H, Mitra S, Biswas D, Wattam AR, Letvin NL, and Jacobs WR Jr (2014). Noncanonical SMC protein in *Mycobacterium smegmatis* restricts maintenance of *Mycobacterium fortuitum* plasmids. *Proc. Natl. Acad. Sci. U. S. A* 111, 13264–13271. [PubMed: 25197070]
- Perez-Riverol Y, Bai J, Bandla C, García-Seisdedos D, Hewapathirana S, Kamatchinathan S, Kundu DJ, Prakash A, Frericks-Zipper A, Eisenacher M, et al. (2022). The PRIDE database resources in 2022: a hub for mass spectrometry-based proteomics evidences. *Nucleic Acids Res.* 50, D543–D552. [PubMed: 34723319]

- Petrushenko ZM, She W, and Rybenkov VV (2011). A new family of bacterial condensins. *Mol. Microbiol* 81, 881–896. [PubMed: 21752107]
- Petterson EF, Goddard TD, Huang CC, Couch GS, Greenblatt DM, Meng EC, and Ferrin TE (2004). UCSF Chimera—a visualization system for exploratory research and analysis. *J. Comput. Chem* 25, 1605–1612. [PubMed: 15264254]
- Petterson EF, Goddard TD, Huang CC, Meng EC, Couch GS, Croll TI, Morris JH, and Ferrin TE (2021). UCSF ChimeraX: Structure visualization for researchers, educators, and developers. *Protein Sci.* 30, 70–82. [PubMed: 32881101]
- Pradhan B, Kanno T, Igarashi MU, Baaske MD, Wong JSK, Jeppsson K, Björkegren C, and Kim E (2022). The Smc5/6 complex is a DNA loop extruding motor. *bioRxiv* DOI: 10.1101/2022.05.13.491800
- Punjani A, Rubinstein JL, Fleet DJ, and Brubaker MA (2017). cryoSPARC: algorithms for rapid unsupervised cryo-EM structure determination. *Nat. Methods* 14, 290–296. [PubMed: 28165473]
- Rajasekar KV, Baker R, Fisher GLM, Bolla JR, Mäkelä J, Tang M, Zawadzka K, Koczy O, Wagner F, Robinson CV, et al. (2019). Dynamic architecture of the Escherichia coli structural maintenance of chromosomes (SMC) complex, MukBEF. *Nucleic Acids Res.* 47, 9696–9707. [PubMed: 31400115]
- Roth S, Rottach A, Lotz-Havla AS, Laux V, Muschaweckh A, Gersting SW, Muntau AC, Hopfner K-P, Jin L, Vanness K, et al. (2014). Rad50-CARD9 interactions link cytosolic DNA sensing to IL-1 β production. *Nat. Immunol* 15, 538–545. [PubMed: 24777530]
- Sanchez-Garcia R, Gomez-Blanco J, Cuervo A, Carazo JM, Sorzano COS, and Vargas J (2021). DeepEMhancer: a deep learning solution for cryo-EM volume post-processing. *Commun Biol* 4, 874. [PubMed: 34267316]
- Schiltz CJ, Lee A, Partlow EA, Hosford CJ, and Chappie JS (2019). Structural characterization of Class 2 OLD family nucleases supports a two-metal catalysis mechanism for cleavage. *Nucleic Acids Res.* 47, 9448–9463. [PubMed: 31400118]
- Schindelin J, Arganda-Carreras I, Frise E, Kaynig V, Longair M, Pietzsch T, Preibisch S, Rueden C, Saalfeld S, Schmid B, et al. (2012). Fiji: an open-source platform for biological-image analysis. *Nat. Methods* 9, 676–682. [PubMed: 22743772]
- Shaltiel IA, Datta S, Lecomte L, Hassler M, Kschonsak M, Bravo S, Stober C, Ormanns J, Eustermann S, and Haering CH (2022). A hold-and-feed mechanism drives directional DNA loop extrusion by condensin. *Science* 376, 1087–1094. [PubMed: 35653469]
- Shi Z, Gao H, Bai X-C, and Yu H (2020). Cryo-EM structure of the human cohesin-NIPBL-DNA complex. *Science* 368, 1454–1459. [PubMed: 32409525]
- Snapper SB, Melton RE, Mustafa S, Kieser T, and Jacobs WR Jr (1990). Isolation and characterization of efficient plasmid transformation mutants of *Mycobacterium smegmatis*. *Mol. Microbiol* 4, 1911–1919. [PubMed: 2082148]
- Staal J, Alci K, De Schamphelaire W, Vanhoucke M, and Beyaert R (2019). Engineering a minimal cloning vector from a pUC18 plasmid backbone with an extended multiple cloning site. *Biotechniques* 66, 254–259. [PubMed: 31124712]
- Steinegger M, and Söding J (2017). MMseqs2 enables sensitive protein sequence searching for the analysis of massive data sets. *Nat. Biotechnol* 35, 1026–1028. [PubMed: 29035372]
- Stern A, and Sorek R (2011). The phage-host arms race: shaping the evolution of microbes. *Bioessays* 33, 43–51. [PubMed: 20979102]
- Woo J-S, Lim J-H, Shin H-C, Suh M-K, Ku B., Lee K-H, Joo K, Robinson H, Lee J, Park S-Y, et al. (2009). Structural studies of a bacterial condensin complex reveal ATP-dependent disruption of intersubunit interactions. *Cell* 136, 85–96. [PubMed: 19135891]
- Yatskevich S, Rhodes J, and Nasmyth K (2019). Organization of Chromosomal DNA by SMC Complexes. *Annu. Rev. Genet* 53, 445–482. [PubMed: 31577909]
- Zhao H, Bhowmik BK, Petrushenko ZM, and Rybenkov VV (2020). Alternating Dynamics of oriC, SMC, and MksBEF in Segregation of *Pseudomonas aeruginosa* Chromosome. *mSphere* 5, e00238–20. [PubMed: 32907947]

Zheng SQ, Palovcak E, Armache J-P, Verba KA, Cheng Y, and Agard DA (2017). MotionCor2: anisotropic correction of beam-induced motion for improved cryo-electron microscopy. *Nat. Methods* 14, 331–332. [PubMed: 28250466]

Author Manuscript

Author Manuscript

Author Manuscript

Author Manuscript

HIGHLIGHTS

- The Wadjet defense system protects its bacterial host from plasmid transformation
- Wadjet specifically recognizes and cleaves plasmid DNA in a reaction requiring ATP
- Three Wadjet subunits form an SMC-family complex similar to bacterial MukBEF
- Wadjet's nuclease subunit is related to an archaeal type II DNA topoisomerase

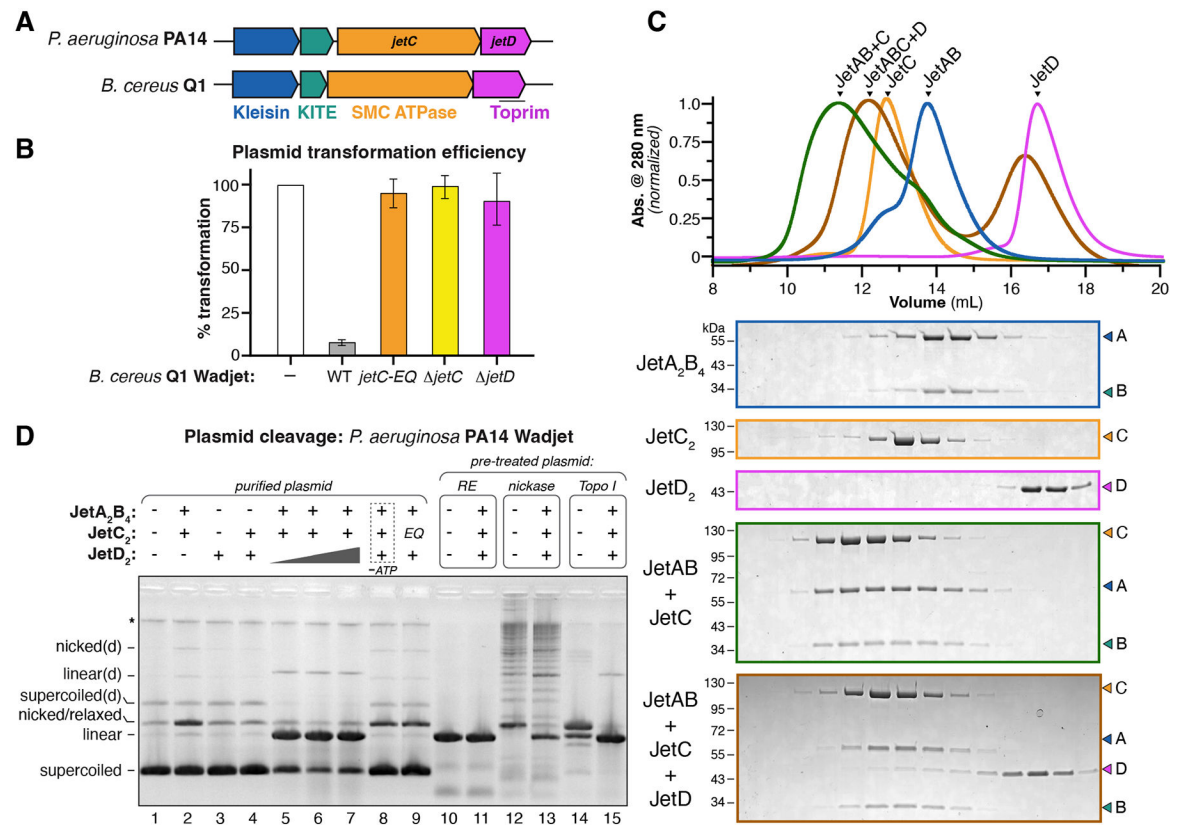


Figure 1. Wadjet specifically cleaves closed-circular DNA

(A) Schematic of Wadjet systems from *P. aeruginosa* PA14 and *B. cereus* Q1. JetA (blue) is predicted to be similar to the MukF kleisin subunit of bacterial MukBEF condensin complexes; JetB (green) is predicted to be similar to MukeE KITE subunit, and JetC (yellow) is predicted to be similar to MukB SMC subunit. JetD (pink) has an N-terminal DUF3322 domain and a C-terminal toprim domain found in topoisomerases and nucleases.

(B) Efficiency of episomal plasmid transformation in *B. subtilis*, in the presence or absence of chromosomally-integrated *B. cereus* Q1 Wadjet or mutants. JetC-EQ: E1025Q Walker B mutation. Bars represent the average and standard deviation of three independent measurements, normalized to 100% efficiency for *B. subtilis* lacking Wadjet (white bar).

(C) Size-exclusion chromatography analysis of reconstituted *P. aeruginosa* PA14 Wadjet subcomplexes. Oligomerization state of each complex was verified by size-exclusion chromatography coupled to multi-angle light scattering (SEC-MALS) (Figure S1).

(D) Cleavage of a supercoiled plasmid by reconstituted *P. aeruginosa* PA14 Wadjet. Separately purified JetA₂B₄, JetC₂, and JetD₂ were added to pUC18 plasmid DNA either separately or together in the presence of ATP, and cleavage was monitored by agarose gel electrophoresis. Major input and product bands are labeled at left with "(d)" indicating dimeric (double-length) plasmid; asterisk (*) denotes contaminant DNA. JetA₂B₄ was used at 210 nM concentration, JetC₂ at 210 nM, and JetD₂ at 210 nM (yielding 105 nM of the putative dimeric JetA₂B₄C₄D₄ in lanes with all components, with an excess of JetA₂B₄). The JetD₂ concentration gradient in lanes 5-7 used 75/150/210 nM JetD₂. Cleavage is compromised in reactions lacking ATP (lane 8) or with a JetC Walker B mutation (E1022Q;

lane 9). Low-level nonspecific nicking is observed in reactions lacking JetD (lane 2), lacking ATP (lane 8), and with a JetC Walker B mutation (E1022Q; lane 9). Lanes 10-11 use pUC18 pre-treated with NdeI to generate linear plasmid; Lanes 12-13 use pUC18 pre-treated with Nt.BsmA1 nicking enzyme to generate nicked/relaxed plasmid; Lanes 14-15 use pUC18 pre-treated with *E. coli* DNA Topoisomerase I to generate relaxed plasmid (three topoisomers visible).

Author Manuscript

Author Manuscript

Author Manuscript

Author Manuscript

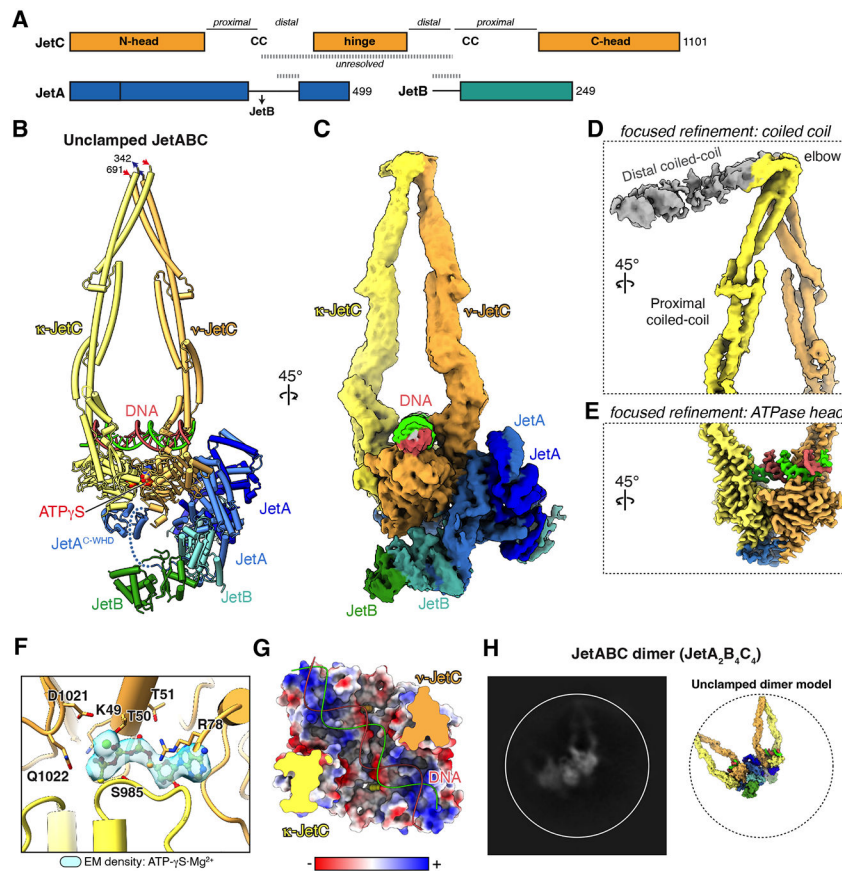


Figure 2. Structure of the JetABC complex

- (A) Domain schematics of *P. aeruginosa* PA14 JetA, JetB, and JetC. Dashed lines indicate regions of each subunit that are unresolved in cryoEM density.
- (B) Cartoon view of a JetA₂B₄C₂ complex in an “unclamped” conformation, with JetA subunits colored light blue/dark blue, JetB (two subunits visible) colored green/cyan, JetC colored orange (ν -JetC) and yellow (κ -JetC), and bound dsDNA colored red/green. The distal coiled-coil and hinge domains of JetC are disordered, as are a short linker between JetA’s JetB-binding region and its C-terminal WHD domain (indicated as a dotted line), and the N-terminal tail of JetB.
- (C) CryoEM density for a JetA₂B₄C₂ complex, colored as in panel (B). See Figure S5 and Table 1 for details.
- (D) CryoEM density from a focused refinement on the JetC coiled-coils, showing disordered density for the distal coiled-coil regions (gray).
- (E) CryoEM density from a focused refinement on the DNA-bound JetC ATPase heads, with the JetA C-WHD visible (blue)
- (F) Closeup view of ATP- γ -S-Mg²⁺ bound to the JetC head, with cryoEM density shown in light blue.
- (G) Top-down view of the JetC heads, with surface colored by electrostatic potential.
- (H) *Left*: One 2D class average from cryoEM analysis of the JetABC complex, showing a dimeric complex with two JetC dimers. *Right*: Model of an unclamped JetABC dimer (with JetA₂B₄C₄ stoichiometry) oriented as in the 2D class at right. The JetABC dimer model

was generated by expanding the observed JetA-JetC interface across the two-fold symmetric JetA dimer.

Author Manuscript

Author Manuscript

Author Manuscript

Author Manuscript

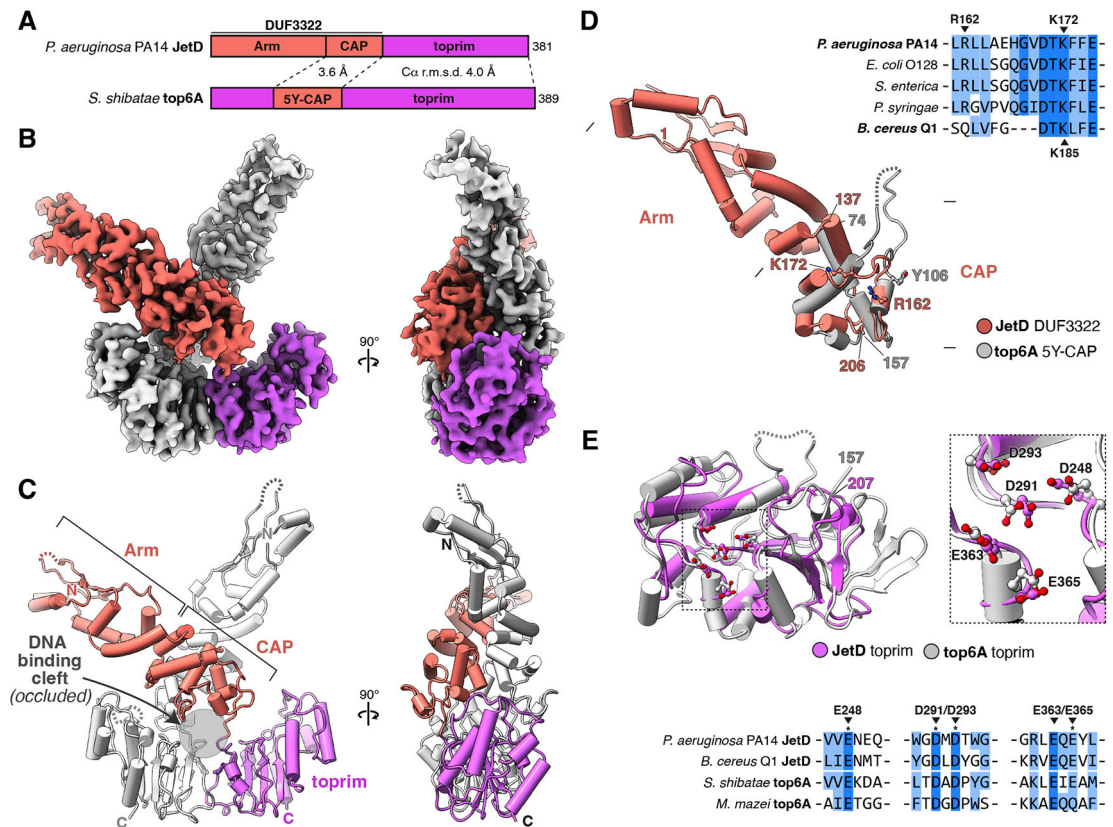


Figure 3. JetD is a diverged topoisomerase-like protein

(A) Domain schematics of *P. aeruginosa* PA14 JetD and *S. shibatae* topoisomerase VI-A (top6A) (PDB ID 2ZBK; (Graille et al., 2008)), with N-terminal domains colored coral and C-terminal toprim domains pink. Distances noted are C α r.m.s.d. values for separate overlays of the C-terminal portion of the DUF3322 domain (residues 138-206 of JetD, referred to as CAP) and the toprim domain (residues 207-381).

(B) CryoEM density for a *P. aeruginosa* PA14 JetD dimer, with one subunit colored as in panel (A) and the second light gray. The map shown is a composite of two local-refinement reconstructions focusing on either the N-terminal DUF3322 domain dimer (coral; final resolution 3.45 Å) or the C-terminal toprim domain dimer (pink; 3.61 Å), aligned with a reconstruction of the entire particle (3.69 Å) (Figure S8, Table 1).

(C) Model for the JetD dimer (see Figure S8J-K for agreement between JetD map and model). The N-terminal DUF3322 domain (coral) is labeled as separate Arm and CAP subdomains, and the C-terminal toprim domain is shown in pink. The putative DNA binding cleft is indicated with a gray circle and labeled.

(D) Structural overlay of the JetD DUF3322 domain (coral; Arm and CAP subdomains noted) with the 5Y-CAP domain (gray) of *S. shibatae* top6A (PDB ID 2ZBK; (Graille et al., 2008)). Shown in sticks for JetD are residues R162 and K172, and for top6A is Y106. Sequence alignment shows five JetD homologs with R162 and K172 noted. NCBI sequence accessions for JetD proteins in alignment: *P. aeruginosa* PA14 (EOT10763.1), *E. coli* O128 (KDV63662.1), *S. enterica* (ECI5565369.1), *P. syringae* (WP_122224314.1), *B. cereus* Q1 (ACM11448.1).

(E) Structural overlay of the top6A domains of JetD (pink) and *S. shibatae* top6A (gray; PDB ID 2ZBK; (Graille et al., 2008)). Close-up view and sequence alignment show the conservation of putative active site residues in both proteins. NCBI sequence accessions for proteins in alignment: *P. aeruginosa* PA14 JetD (EOT10763.1), *B. cereus* Q1 JetD (ACM11448.1), *S. shibatae* top6A (WP_218258439.1), *M. mazei* top6A (WP_011034342.1).

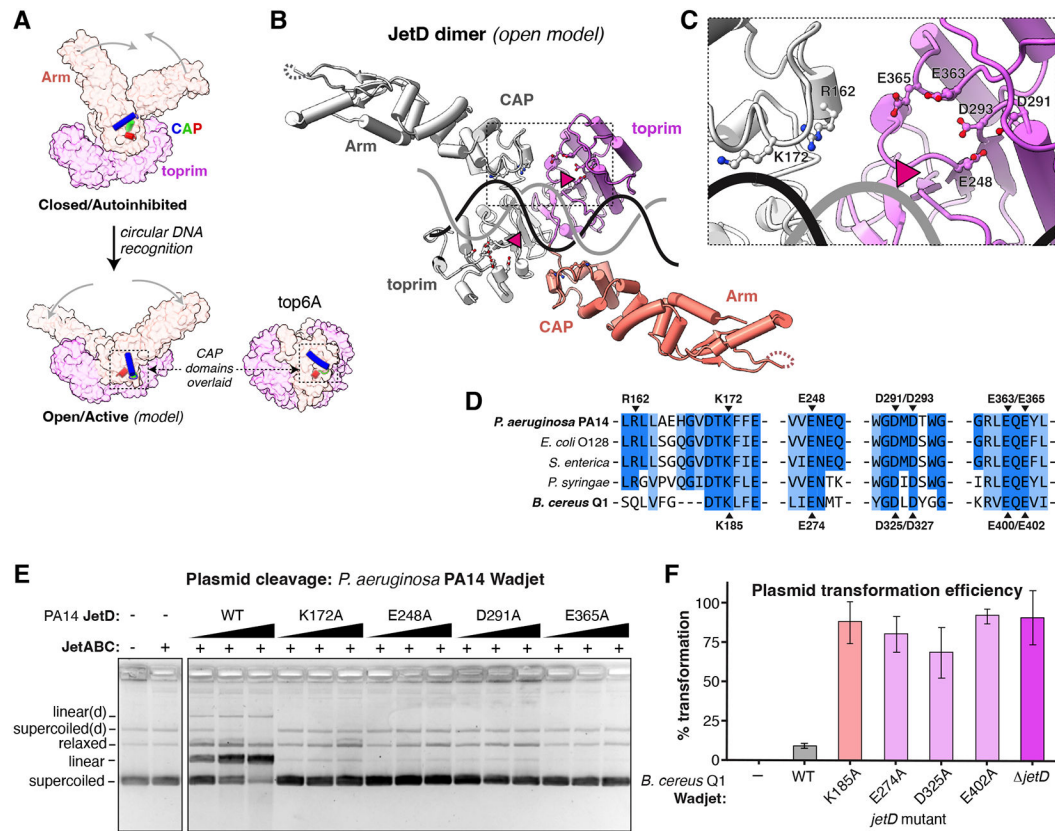


Figure 4. JetD nuclease activity is required for Wadjet function

(A) Schematic depicting the closed, autoinhibited JetD dimer conformation imaged by cryoEM (top) and the proposed open, active conformation (bottom). In the closed state, the DNA-binding pocket and active sites are sterically occluded by the crossed DUF3322 domains (coral). The open conformation was modeled by overlaying conserved elements of the JetD CAP domain (blue/green/red) with the CAP domain of *S. shibatae* top6A (PDB ID 2ZBK; (Graille et al., 2008)).

(B) Top-down view of an open JetD dimer model. Modeled DNA is shown as black/gray lines, with putative DNA cleavage locations positioned at the dimer-related active sites noted with pink arrowheads.

(C) Close-up view of one modeled JetD active site from panel (B), showing that the putative active site in the toprim domain of one JetD protomer (pink) is aligned with the positively-charged residues R162 and K172 in the CAP domain of the opposite JetD protomer.

(D) Sequence alignment of five JetD homologs with conserved active-site residues noted. Top line: *P. aeruginosa* JetD used for biochemical assays (see panel E); Bottom line: *B. cereus* Q1 JetD, used for plasmid transformation assays (see panel F). See legend of Figure 3D for sequence identifiers.

(E) Plasmid DNA (pUC18) cleavage by *P. aeruginosa* PA14 Wadjet, with wild-type or the indicated mutants of JetD.

(F) Plasmid transformation efficiency of *B. subtilis* encoding *B. cereus* Q1 Wadjet with wild-type or mutant JetD. Bars represent the average and standard deviation of three

independent measurements, normalized to 100% efficiency for *B. subtilis* lacking Wadjet (white bar).

Author Manuscript

Author Manuscript

Author Manuscript

Author Manuscript

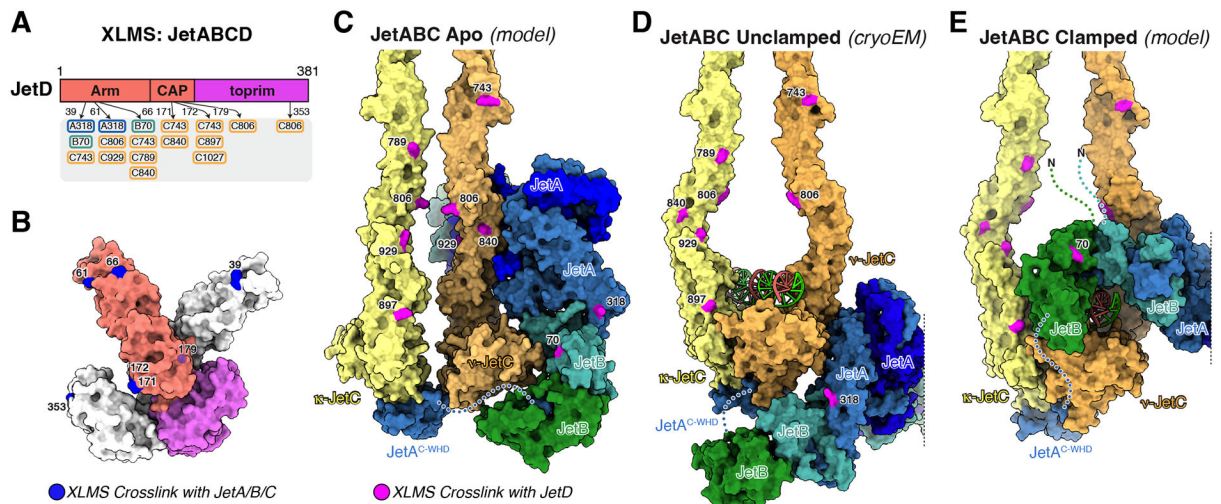


Figure 5. Interactions of JetABC with JetD

(A) Domain schematic of *P. aeruginosa* PA14 JetD with residues that crosslink to JetA/JetB/JetC in crosslinking mass spectrometry (XLMS) experiments noted. Crosslinks to JetA are highlighted in blue, crosslinks to JetB are highlighted in green, and crosslinks to JetC are highlighted in orange (see Figure S7 and **Table 2** for XLMS data).

(B) Structure of the JetD dimer, with one protomer colored as in panel (A) and the other protomer white. Residues that crosslink with JetA/B/C are shown in blue. Residue 179 is buried in the DUF3322 domain dimer interface.

(C) Modeled structure of a JetA₂B₄C₂ complex in an Apo state, based on the structure of the JetA-JetB-JetC^{head} complex (Figure S3), with coiled-coils modeled from the structure of full-length JetABC and the κ -JetC subunit modeled from the structure of MukBEF in the Apo state (PDB ID 7NYY; (Bürmann et al., 2021)). Residues that crosslink with JetD in XLMS experiments are shown in pink and labeled (see Figure S9 and **Table 2** for XLMS data).

(D) Structure of unclamped JetA₂B₂C₂ with residues that crosslink with JetD in XLMS experiments are shown in pink and labeled.

(E) Structure of a modeled “clamped” state of a JetA₂B₂C₂ complex based on a structure of MukBEF in the clamped state (PDB ID 7NYX; (Bürmann et al., 2021)). Residues that crosslink with JetD are colored pink and labeled. The positions of the disordered JetB N-terminal tails are shown as dotted lines.

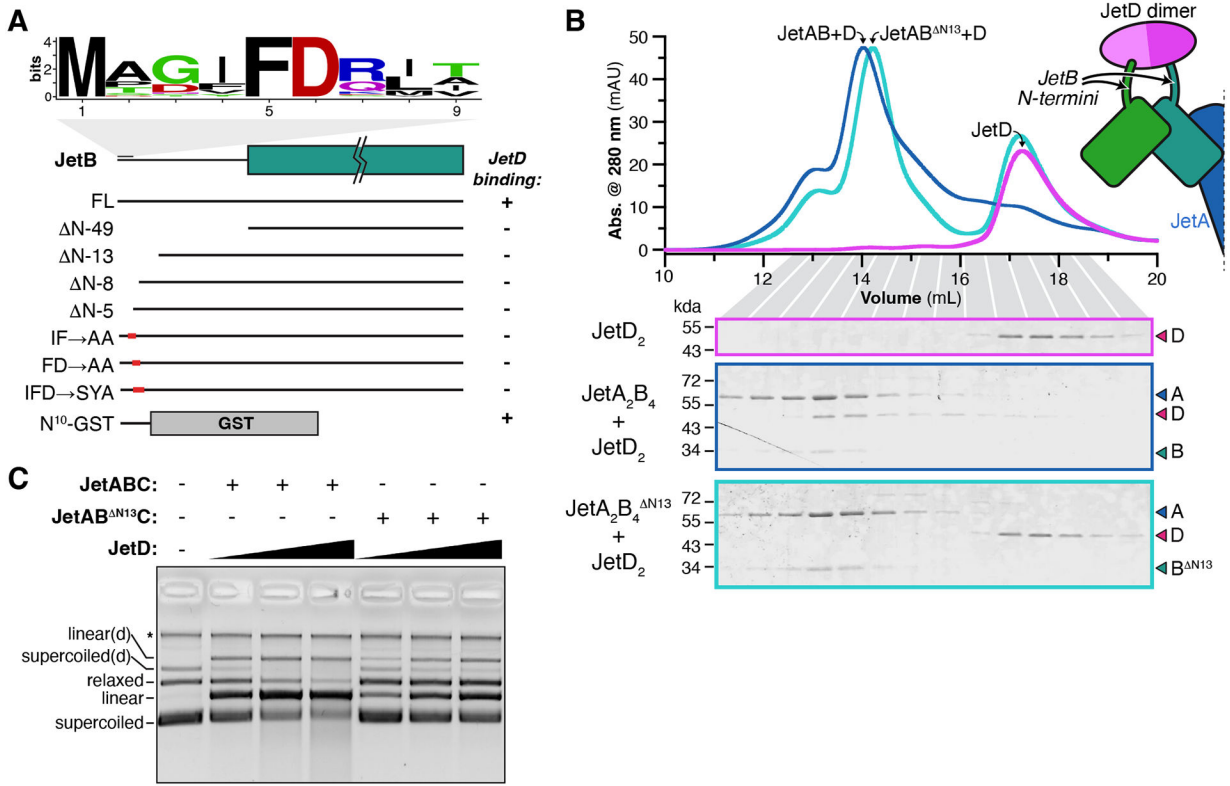


Figure 6. The JetB N-terminus interacts with JetD

(A) Top: Domain schematic of *P. aeruginosa* JetB, with sequence logo showing conservation of an IFDR motif in residues 4-7 of the JetB N-terminal tail. Bottom: Summary of interaction assays measuring association of JetD with JetAB complexes with the noted truncations or mutations in the JetB N-terminus (Figure S10A-C). The gray box denotes constructs that interact with JetD (+) and those that do not (-).

(B) Size-exclusion chromatography of JetD (top: pink), JetAB + JetD (middle: blue), and JetAB^{N13} (bottom, teal). JetD binds and co-elutes with full-length JetAB, but not JetAB^{N13}. See Figure S10A for similar experiments with other JetB truncations and mutations in the IFDR motif, and Figure S10C for JetD binding a JetB-N10:GST fusion protein. *Right inset*: Schematic of JetB N-termini binding JetD.

(C) Plasmid DNA cleavage by the *P. aeruginosa* PA14 wild-type Wadjet complex and a complex that lacks JetB JetD interactions. JetD concentration gradients include 105 nM JetA₂B₄C₄ complex and 75/150/210 nM JetD₂. Asterisk (*) denotes contaminant DNA.

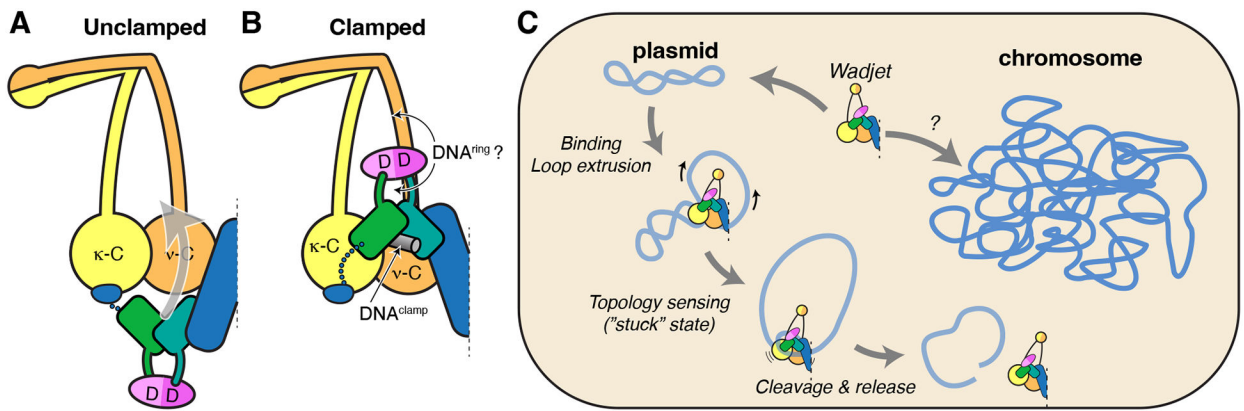


Figure 7. Model for Wadjet assembly, DNA binding, and plasmid restriction

(A) Schematic model of a JetAB₂C₂ complex in an unclamped state. Dotted line indicates that this schematic represents half of the full JetA₂B₄C₄ dimer complex observed in solution.

(B) Schematic model of a JetAB₂C₂ complex in a clamped state, bound to clamp-site DNA (DNA^{clamp}) shown in gray. Two possible locations for a second DNA (ring-site; DNA^{ring}) are indicated by arrows.

(C) Model for Wadjet-mediated plasmid restriction in cells. After a plasmid enters the cell, Wadjet binds the plasmid and extrudes a DNA loop. If the substrate DNA is a closed circle, loop extrusion will stall and the resulting “stuck” state will cause recruitment and/or activation of JetD-mediated DNA cleavage. Wadjet is likely able to bind and extrude loops on chromosomal DNA, but may be prevented from cleaving the chromosome by not entering the “stuck” state.

Table 1.

CryoEM data collection, reconstruction, and refinement statistics

	A ₂ B ₄ C ^{head} ₂ EMDB 27480 PDB 8DK1	JetC ₂ head EMDB 27482 PDB 8DK3	JetC ₂ FL	JetA ₂ B ₄ C ₂ EMDB 27481 PDB 8DK2	JetD NTD	JetD CTD	JetD FL EMDB 25913 PDB 7TIL
Data collection and processing							
Microscope	Titan Krios G3	Titan Krios G3			Titan Krios G3		
Voltage (kV)	300	300			300		
Nominal magnification	165,000	130,000			215,000		
Detector	Gatan K2	Gatan K2			Gatan K2		
Pixel size (Å)	0.84	1.10			0.65		
GIF slit-width (eV)	20	20			20		
Fluence (e ⁻ /Å ²)	54.1	50.1			62		
Nominal defocus range (µm)	-0.5 to -2.5	-0.5 to -2.5			-0.5 to -2.5		
Movies collected	1280	3094			1225		
Symmetry imposed	C2	C1	C1	C1	C1	C1	C1
Final particles (no.)	130,904	323,026	176,564	56,600	51,336	51,336	51,336
Resolution (FSC _{0.143} , Å)	2.95	3.28	3.78	4.08	3.45	3.61	3.69
Local Resolution range 25 th -75 th percentile (FSC _{0.143} , Å)	2.77-5.22	2.98-5.31	4.49-7.26	4.98-7.94	3.12 to 5.14	3.25 to 4.91	3.58 to 6.96
Model							
Model Composition							
Protein residues	2446	999	1535	2840	400	335	739
Ligands	n.a.	2 ATP-γ-S	2 ATP-γ-S	2 ATP-γ-S	n.a.	n.a.	n.a.
	n.a.	2 Mg ²⁺	2 Mg ²⁺	2 Mg ²⁺			
	n.a.	52 Nucleotides	52 Nucleotides	52 Nucleotides			
Isotropic ADPs (Å ²)							
Protein	132.6	143.9	223.9	359.4	122.1	144.8	124.2
Ligands	n.a.	127.5	109.3	85.5	n.a.	n.a.	n.a.
Nucleotides	n.a.	233.1	206.4	162.1	n.a.	n.a.	n.a.
Map Correlation Coefficient	0.90	0.86	0.85	0.80	0.85	0.84	0.84
Resolution (FSC _{0.5} , Å)	3.2	3.5	4.0	4.3	3.6	4.0	3.8
RMSDs							
Bond lengths (Å)	0.002	0.006	0.003	0.002	0.003	0.002	0.002
Bond angles (°)	0.42	0.579	0.531	0.465	0.660	0.537	0.537
Validation							
Molprobrity score	1.40	1.59	1.89	2.02	1.68	1.50	1.69
Clashscore	2.83	3.66	9.67	7.70	8.77	6.54	7.86
Poor rotamers (%)	1.44	0.85	0.86	2.88	0	0	0
EMRinger score	2.70	2.42	1.11	0.93	1.85	2.63	1.83

	A₂B₄C^{head}₂ EMDB 27480 PDB 8DK1	JetC₂ head EMDB 27482 PDB 8DK3	JetC₂ FL	JetA₂B₄C₂ EMDB 27481 PDB 8DK2	JetD NTD	JetD CTD	JetD FL EMDB 25913 PDB 7TIL
Ramachandran (%)							
Favored	96.74	93.20	94.41	96.32	96.68	97.26	96.16
Allowed	3.26	6.80	5.59	3.68	3.32	2.74	3.84
Disallowed	0	0	0	0	0	0	0

KEY RESOURCES TABLE

REAGENT or RESOURCE	SOURCE	IDENTIFIER
Bacterial and virus strains		
<i>Bacillus subtilis</i>	(Doron et al., 2018)	BEST7003
<i>Bacillus subtilis</i> + <i>B. cereus</i> Wadjet Q1 (WT)	This paper	N/A
<i>Bacillus subtilis</i> + <i>B. cereus</i> Wadjet JetC(E1025Q)	This paper	N/A
<i>Bacillus subtilis</i> + <i>B. cereus</i> Wadjet JetC	This paper	N/A
<i>Bacillus subtilis</i> + <i>B. cereus</i> Wadjet JetD	This paper	N/A
<i>Bacillus subtilis</i> + <i>B. cereus</i> Wadjet JetD(K185A)	This paper	N/A
<i>Bacillus subtilis</i> + <i>B. cereus</i> Wadjet JetD(E274A)	This paper	N/A
<i>Bacillus subtilis</i> + <i>B. cereus</i> Wadjet JetD(D325A)	This paper	N/A
<i>Bacillus subtilis</i> + <i>B. cereus</i> Wadjet JetD(E402A)	This paper	N/A
<i>Bacillus subtilis</i> + empty vector	This paper	N/A
<i>E. coli</i> Rosetta2 pLysS	EMD Millipore	71403
Biological samples		
Genomic DNA from <i>P. aeruginosa</i> strain PA14	J. Pogliano	PA14
Chemicals, peptides, and recombinant proteins		
NdeI	New England Biolabs	R0111S
Nt.BsmAI	New England Biolabs	R0121S
<i>E. coli</i> DNA topoisomerase I	New England Biolabs	M0301S
ATP- γ -S	Sigma Aldrich	11162306001
BS3-H12/D12 crosslinker	Creative Biomolecules	001SS
TEV protease	(Kapust et al., 2001)	pRK793 (Addgene #8827)
Sequencing-grade trypsin	Promega	V5111
T4 DNA polymerase	New England Biolabs	M0203S
T4 Polynucleotide kinase	New England Biolabs	M0201S
EcoRV-HF	New England Biolabs	R3195S
Calf intestinal phosphatase	New England Biolabs	M0525S
Critical commercial assays		
ADP-Glo kinase assay	Promega	V6930
Deposited data		
JetA-JetB-JetC ^{head} cryoEM reconstruction	This paper	EMDB: 27480
JetA-JetB-JetC ^{head} model coordinates	This paper	PDB: 8DK1

REAGENT or RESOURCE	SOURCE	IDENTIFIER
JetABC FL cryoEM reconstruction	This paper	EMDB: 27481
JetABC FL model coordinates	This paper	PDB: 8DK2
JetC:JetA ^{cWHD} cryoEM reconstruction	This paper	EMDB: 27482
JetC:JetA ^{cWHD} Model coordinates	This paper	PDB: 8DK3
JetD cryoEM reconstruction	This paper	EMDB: 25913
JetD model coordinates	This paper	PDB: 7TIL
JetABCD XL-MS raw data and processed files	This paper	PRIDE: PXD031096
Mendeley data (Uncropped annotated gel images)	This paper	http://dx.doi.org/10.17632/x9923grfjw.1
Oligonucleotides		
GTGATAGTTAGAAACGTAATTGACTATAAAGATGATGACGATAAGTAGGATGTCTATAGACCAGG	IDT	JetABC_cryo_Fwd
CCTGGTCTATAGACATCCTACTTATCGTCATCATCTTTATAGTCAATTACGTTTCTAACTATCAC	IDT	JetABC_cryo_Rev
Recombinant DNA		
pSG1-rfp plasmid vector (<i>Bacillus</i> integration vector)	(Doron et al., 2018)	pSG1-rfp
pSG1-Wadjet	(Doron et al., 2018)	pSG1-Wadjet
pUC1057 plasmid	This paper	N/A
pUC18 plasmid	Thermo Fisher	SD0051
pBS42 plasmid for transformation assay	Bacillus Genetic Stock Center	ECE10
UC Berkeley Macrolab vector 2-AT	Addgene	29665
UC Berkeley Macrolab vector 2-BT	Addgene	29666
UC Berkeley Macrolab vector 13S-A	Addgene	48323
Software and algorithms		
cryoSPARC	Structura Biotechnology	version 3.2
ChimeraX	(Pettersen et al., 2021)	version 1.3
Fiji	(Schindelin et al., 2012)	version 2.1.0
GraphPad Prism	GraphPad Software	version 9
ASTRA	Wyatt Technology	version 8
ISOLDE	(Croll, 2018)	https://isolde.cimr.cam.ac.uk/
Phenix	(Afonine et al., 2018)	version 1.20.1
COOT	(Emsley et al., 2010)	version 0.9
ColabFold	(Mirdita et al., 2022)	https://github.com/sokrypton/ColabFold

REAGENT or RESOURCE	SOURCE	IDENTIFIER
msConvert	(Adusumilli and Mallick, 2017)	version 3.0
xVis Webserver	(Grimm et al., 2015)	https://xvis.genzentrum.lmu.de/
xQuest/xProphet	(Leitner et al., 2014)	https://gitlab.ethz.ch/leitner_lab/xquest_xprophet
Xlink Analyzer Plug-in	(Kosinski et al., 2015)	https://www.embl-hamburg.de/XlinkAnalyzer/XlinkAnalyzer.html
Other		
HisTrap HP column	Cytiva	17524801
HiTrap Q HP column	Cytiva	17115401
Glutathione Agarose Pierce	Thermo Scientific	16101
Superose 6 Increase 10/300 GL column	Cytiva	29091596
Superdex 30 Increase 10/300 GL column	Cytiva	29219757
Superdex 200 Increase 10/300 GL column	Cytiva	10266446
Sep-Pak C18 cartridge	Waters	WAT043410
Zeba Spin Desalting Columns (7K MWCO)	Thermo Fisher Scientific	89882

Author Manuscript

Author Manuscript

Author Manuscript

Author Manuscript